



Article

Linking Turbulent Interplanetary Magnetic Field Fluctuations and Current Sheets

Maria O. Riazantseva¹, Timofey V. Treves^{1,2}, Olga Khabarova^{3,*}, Liudmila S. Rakhmanova¹, Yuri I. Yermolaev¹
and Alexander A. Khokhlachev¹

¹ Space Research Institute, Russian Academy of Sciences (IKI), Moscow 117997, Russia; m.riazantseva@cosmos.ru (M.O.R.); treves@izmiran.ru (T.V.T.); aleks.xaa@yandex.ru (A.A.K.)

² Pushkov Institute of Terrestrial Magnetism, Ionosphere and Radiowave Propagation of the Russian Academy of Sciences (IZMIRAN), Moscow 108840, Russia

³ Raymond & Beverly Sackler Faculty of Exact Sciences, Tel Aviv University, Tel Aviv 6139001, Israel

* Correspondence: olgakhabar@tauex.tau.ac.il

Abstract: The study aims to understand the role of solar wind current sheets (CSs) in shaping the spectrum of turbulent fluctuations and driving dissipation processes in space plasma. Local non-adiabatic heating and acceleration of charged particles in the solar wind is one of the most intriguing challenges in space physics. Leading theories attribute these effects to turbulent heating, often associated with magnetic reconnection at small-scale coherent structures in the solar wind, such as CSs and flux ropes. We identify CSs observed at 1 AU in different types of the solar wind around and within an interplanetary coronal mass ejection (ICME) and analyze the corresponding characteristics of the turbulent cascade. It is found that the spectra of fluctuations of the interplanetary magnetic field may be reshaped due to the CS impact potentially leading to local disruptions in energy transfer along the cascade of turbulent fluctuations. Case studies of the spectra behavior at the peak of the CS number show their steepening at MHD scales, flattening at kinetic scales, and merging of the spectra into a single form, with the break almost disappearing. In the broader vicinity of the CS number peak, the behavior of spectral parameters changes sharply, but not always following the same pattern. The statistical analysis shows a clear correlation between the break frequency and the CS number. These results are consistent with the picture of turbulent reconnection at CSs. The CS occurrence is found to be statistically linked with the increased temperature. In the ICME sheath, there are two CS populations observed in the hottest and coldest plasma.

Keywords: solar wind; current sheets; turbulence; plasma heating



Citation: Riazantseva, M.O.; Treves, T.V.; Khabarova, O.; Rakhmanova, L.S.; Yermolaev, Y.I.; Khokhlachev, A.A. Linking Turbulent Interplanetary Magnetic Field Fluctuations and Current Sheets. *Universe* **2024**, *10*, 417. <https://doi.org/10.3390/universe10110417>

Academic Editor: Pablo S. Moya

Received: 5 September 2024

Revised: 14 October 2024

Accepted: 31 October 2024

Published: 7 November 2024



Copyright: © 2024 by the authors. Licensee MDPI, Basel, Switzerland. This article is an open access article distributed under the terms and conditions of the Creative Commons Attribution (CC BY) license (<https://creativecommons.org/licenses/by/4.0/>).

1. Introduction

One of the central unresolved issues in space physics is the unexpected solar wind heating, as observed through in situ measurements from various spacecraft. The radial evolution of solar wind temperature deviates from theoretical predictions, indicating the presence of an additional heating source within the heliospheric plasma, beyond the solar corona (e.g., [1–4]). For instance, Kislov et al. [3] have demonstrated that the solar wind temperature measured by the Voyager spacecraft remains nearly constant from 2 AU to 10 AU, decreasing with heliocentric distance in a manner inconsistent with both adiabatic and isothermal processes.

A widely accepted explanation for this phenomenon is the concept of plasma heating through turbulent dissipation (e.g., [5–8]). For example, Adhikari et al. [9] show that the observed radial profile of the solar wind temperature can be determined by peculiarities of the turbulence development at different heliocentric distances. The link between turbulence and temperature is often attributed to heating via waves (see [10–12] and references therein) or by current sheets and discontinuities (e.g., [13,14]).

Current sheets in the solar wind are thin magneto-plasma structures carrying the electric current formed where the local magnetic field undergoes significant directional changes, sometimes even reversing completely. This suggests the presence of a so-called zero magnetic field surface at the center of each current sheet. Current sheets generated by solar wind turbulence are typically small-scale and short-lived, whereas long-lived, large-scale current sheets are formed at the boundaries of high-speed streams and flows, as well as represent extensions of large-scale neutral lines of the solar magnetic field (see [15–18]). These discontinuities play a crucial role in solar wind dynamics by inducing instabilities and altering the magnetic field geometry. A substantial body of research in heliospheric physics has focused on dynamical processes in current sheets (e.g., [19–25]), with discussions increasingly emphasizing their role in the turbulent cascade of the solar wind and the terrestrial magnetosheath (e.g., [26–29]). Many researchers recognize a strong link between current sheets, waves, and turbulence (e.g., [14,28,30–34]). This connection is logical, as a higher number of current sheets leads to an increased turbulence level since current sheets in the solar wind experience magnetic reconnection.

Reconnecting current sheets may contribute to plasma heating, particle acceleration, and the generation of waves and secondary coherent structures in their vicinity since current sheets are known to be sites where magnetic reconnection occurs, converting magnetic energy into the kinetic energy of charged particles. This process is considered as a key mechanism for heating and accelerating particles in the solar corona [35] and can similarly be applied to the solar wind [17,21,22]. Ongoing magnetic reconnection increases the turbulence level in the solar wind, which should be evident in the magnetic field spectra. Indeed, it has been proven that the presence of current sheets determines the shape of the magnetic field variation power spectrum in the solar wind and terrestrial magnetosheath (see [26,27,36–38]). This indicates that current sheets are linked to turbulence, and, in turn, turbulence is associated with plasma heating in the heliosphere on both small and large scales.

Khabarova et al. [39] confirms this point by finding that the daily rate of current sheets at 1 AU, which dynamically varies from hundreds to thousands per day, is proportional to the sum of kinetic and thermal energy density $R \sim V^2(N + 5N') + 10T(N + N')$, where T is the solar wind temperature, V is the solar wind speed, N is the solar wind density, and $N' = 2 \text{ cm}^{-3}$ is the background level of N . The correlation between R and T is stronger than that between R and V , which illustrates the link between the occurrence of current sheets in the solar wind plasma and heating.

Over the past few decades, significant progress has been made in understanding the characteristics of turbulent fluctuations in the solar wind, aided by advancements in experimental techniques that enable increasingly precise measurements of the interplanetary magnetic field (IMF) and solar wind plasma parameters, coupled with enhanced big data processing capabilities. The growing volume of experimental data has facilitated detailed investigations into the turbulent fluctuation spectra at ion-kinetic scales for both IMF fluctuations and solar wind plasma parameters (e.g., [40–44]). Additionally, some works show an analysis of the IMF fluctuation spectra at electron scales [45–48].

It has been believed for a long time that the solar wind exhibits developed turbulence, as suggested in several theoretical models [49]. Recently, Telloni et al. [50] employed Parker Solar Probe and Solar Orbiter observations to show that closer to the Sun (at ~ 0.1 AU), turbulence is observed in the undeveloped state, while it becomes developed with increasing heliocentric distance. Meanwhile, this conclusion requires thorough studies, since the degree of development of turbulence strongly depends on the solar wind type [51–53]. The results of some works indicate that at MHD scales, the solar wind spectrum has a slope of approximately $-5/3$ (e.g., [40,41]), corresponding to Kolmogorov turbulence, which has been shown to be applicable to magnetohydrodynamic flows as well [54]. At kinetic scales, there is sometimes alignment with the theory of kinetic Alfvén wave turbulence, which predicts a spectral slope of $-7/3$ [55]. However, more often, spectra with a slope of ~ -2.8 are observed [40], which are closer to predictions from models accounting for the

contribution of two-dimensional coherent structures with a slope of $\sim -8/3$ [56] or those considering Landau damping [57].

Results of recent studies indicate that solar wind turbulence cannot be considered fully developed, as its evolution is fundamentally constrained by various discontinuities frequently observed in the solar wind, such as shock waves, current sheets, and pressure-balanced structures [52,53,58,59]. Consequently, the spectra of turbulent fluctuations in the solar wind often diverge from those predicted by theoretical models. It has also been shown that the fluctuation spectra exhibit significantly steeper slopes at kinetic scales compared to theoretical predictions in regions of compressed and turbulent plasma, such as those formed downstream of interplanetary shocks driven by interplanetary coronal mass ejections (ICMEs) and in stream- or co-rotating interaction regions (SIRs/CIRs) representing the edges of high-speed streams from coronal holes [60]. This discrepancy may reflect an imbalance in energy transfer across the spectrum, leading to increased dissipation rates and, consequently, heating in these regions.

It should be noted that analyzing the characteristics of fluctuation spectra does not fully answer the question on which structures are primarily responsible for dissipation in each individual case. Taking into account that Khabarova et al. [39] showed that peaks in the number of current sheets per day coincide with the detection of ICME sheaths and SIRs/CIRs at 1 AU, one may suggest that current sheets significantly contribute to dissipation processes in the solar wind, leading to plasma heating, and play a key role in forming the cascade, particularly in the compressed and turbulent plasma, which cannot be said about other types of solar wind.

Most studies on solar wind current sheets have been limited to individual cases or modeling efforts, largely due to the lack of a sufficiently large database suitable for a statistical analysis. To fill this gap, Khabarova et al. [18,39] developed an automated method for identifying current sheets based on the typical behavior of the IMF and plasma parameters at these discontinuities. This led to the creation of the world's largest database of current sheets at 1 AU, containing millions of identified current sheets (<https://csdb.izmiran.ru/>, accessed on 1 November 2024).

In this work, we identify current sheets over an extended time period associated with different solar wind conditions, both within and outside an ICME at Earth's orbit, employing the method proposed by Khabarova et al. [39]. We analyze turbulence characteristics in the solar wind plasma with varying speeds, comparing the number of current sheets with the properties of the turbulent cascade associated with different states of the solar wind. This approach allows us to explore whether the properties of IMF turbulent fluctuations are linked to current sheets and help to better understand the role of current sheets in the anomalous dissipation observed in certain types of solar wind flows.

2. Materials and Methods

We analyze the properties of solar wind plasma and the IMF using an ICME and the surrounding undisturbed solar wind as a set of samples. Figure 1a illustrates the plasma conditions both within and outside the typical ICME in interplanetary space. From left to right, the evolution of the ICME as it propagates through interplanetary space is depicted. The process begins with the formation of a supersonic and super-Alfvénic ICME-driven forward shock followed by a wake, commonly known as the ICME sheath. Closer to the Sun, the magnetic cloud exhibits a regular structure of magnetic field lines wound around a large-scale flux rope. As the ICME moves further into the solar wind, its parts become increasingly turbulent and intermittent, and the magnetic cloud undergoes internal magnetic reconnection, leading to the formation of more complex twisted flux rope structures. This process is often intensified by the interaction of the ICME with other flows, streams, and large-scale structures in the surrounding solar wind (see [17]). The final sketch on the right represents the state of the ICME as it is typically observed at 1 AU, characterized by significantly entangled flux ropes in a fragmented magnetic cloud, with several strong current sheets inside the ICME sheath.

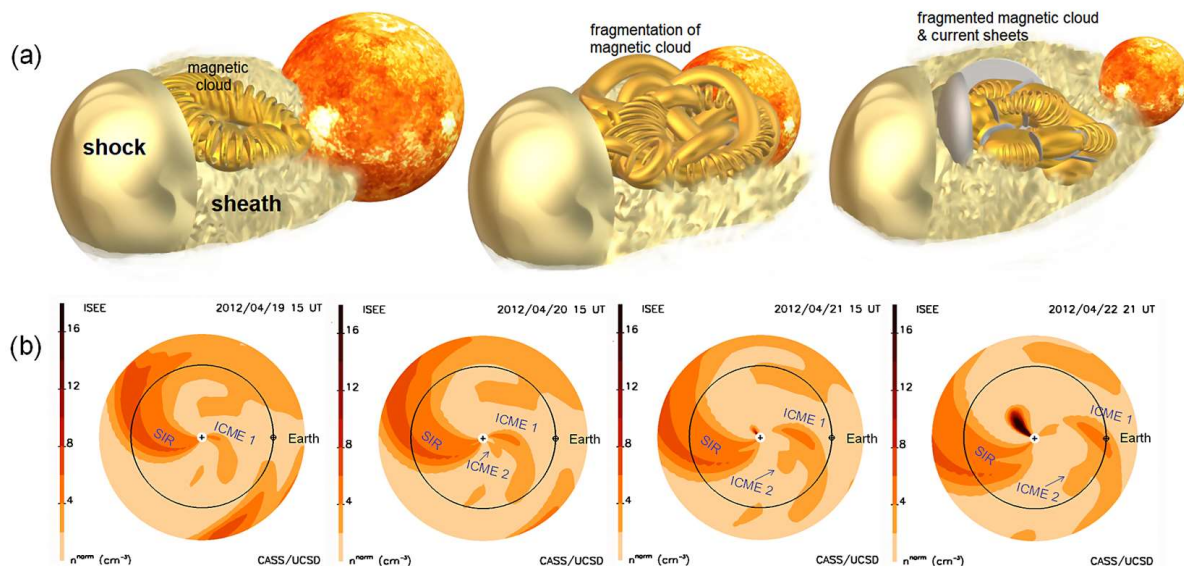


Figure 1. Propagation of ICME in interplanetary space. (a) Structure of ICME on its way from the Sun to the Earth, adapted from Khabarova et al. [17]. (b) Evolution of two merged ICMEs detected at the Earth's orbit on 22–23 April 2012 as reconstructed with interplanetary scintillation measurements.

The link between solar wind compression and heating has been recognized since Elliott et al. [61] first identified this effect in ICMEs. Over the past two decades, it has become evident that the ICME sheath region, located downstream of the interplanetary forward shock, is not only compressed but also turbulent and populated with small-scale coherent structures, such as current sheets and flux ropes—often referred to as magnetic islands in single-point spacecraft measurements [62–65]. Particle heating and acceleration in this region are attributed to processes related to magnetic reconnection at current sheets and the merging (coalescence) of magnetic islands within the compressed plasma region. Additionally, further heating and localized particle acceleration can occur within the fragmented magnetic cloud (e.g., [23]), although the heating rate in the ICME sheath consistently remains higher. Merging of two ICMEs on their way from the Sun significantly enhances the processes and creates a wide and complex ICME sheath with clear signatures of heating presumably associated with enhanced magnetic reconnection (e.g., [64,66]).

The solar wind is not a uniform plasma flowing at different speeds, but rather a collection of distinct flows and streams originating from various regions of the Sun, each with its own properties. These streams generally do not mix, meaning the solar wind can be treated as a composite of different plasmas, which is very useful for the analysis of various dynamic processes developing under different conditions. Every ICME contains several distinct parts, each with unique characteristics. In our study, we deliberately select a complex case of an ICME resulting from the interaction of two CMEs. This ICME comprises a strong interplanetary shock, a wide sheath of the highly increased density and structural complexity, and two distinct magnetic clouds, one of which is highly fragmented due to the CME–CME interaction. The interaction process is illustrated in Figure 1b. The series of reconstructed maps showing the in-ecliptic solar wind's normalized density is provided by the Solar Group at the Center for Astrophysics and Space Sciences, University of California, San Diego, US, based on near-real-time interplanetary scintillation observations from the Institute for Space-Earth Environmental Research (ISEE), Nagoya University, Japan (<https://ips.ucsd.edu/>, accessed on 1 November 2024). These reconstructions, derived from a kinematic model, allow us to link dynamic processes in interplanetary space with the ICME structure observed in situ by spacecraft at the 1st Lagrange point. In the reconstructed density maps, SIRs or longer-lived CIRs appear as elongated sleeves connected to their solar source, while ICMEs typically resemble half-circles, often already disconnected from the Sun by the time they reach Earth's orbit, as depicted in Figure 1b. Note that in the case

of ICMEs, the intense-colored regions practically describe the evolution of the compressed ICME sheath. The maps in Figure 1b show that the large-scale, Earth-directed ICME 1, with a skewed front, opposes the SIR, and then ICME 2 emerges, propagating in nearly the same direction as ICME 1. The two ICMEs merge at an early stage and propagate together to 1 AU, where they are detected by the WIND spacecraft.

The data employed in this study have been collected from the 1 AU WIND spacecraft from the CDAWeb database (<https://cdaweb.gsfc.nasa.gov>, accessed on 1 November 2024) for the period from 22 April 2012, 23:00, to 23 April 2012, 23:00. This interval encompasses the ICME event shown in Figure 1b that can be found in all WIND ICME catalogs, including the IKI catalog <http://iki.rssi.ru/pub/omni/catalog/2012/20120422c.jpg> (accessed on 1 November 2024), [67], the Wind spacecraft ICME catalog https://wind.nasa.gov/ICME_catalog/ICME_catalog_viewer.php (accessed on 1 November 2024) [68], and the University of Science and Technology of China catalog https://space.ustc.edu.cn/dreams/wind_icmes/ (accessed on 1 November 2024).

The interval under investigation is rather long (24 h) and can be separated into several parts characterizing different states of the solar wind:

1. The slow undisturbed solar wind in front of the merged ICME (from the start of the period until 02:15 on 23 April 2012);
2. The ICME-driven shock observed at 02:15 on 23 April 2012, according to the interplanetary shock database <https://ipshocks.helsinki.fi/> (accessed on 1 November 2024);
3. The classic ICME sheath observed from 02:15 to 08:35 on 23 April 2012;
4. The disturbed segment that can be attributed to the mixed sheath–magnetic cloud region formed as a result of the CME–CME interaction (from 08:35 to 17:00 on 23 April 2012). For simplicity, we call this region the “magnetic cloud 1” (MC1).
5. The classic magnetic cloud observed from 16:48 on 23 April 2012 (according to the official Wind spacecraft ICME catalog https://wind.nasa.gov/ICME_catalog/ICME_catalog_viewer.php, accessed on 1 November 2024) to the end of the interval. This region is called below the “magnetic cloud 2” (MC2).

This allows for tracking changes in turbulence characteristics and conditions for current sheet formation across different types of solar wind flows.

The analysis carried out in this study utilizes solar wind plasma parameters (the flow speed, density, temperature, and proton velocity vector) measured by the SWE instrument [69] with a resolution of ~ 99 s, as well as the 3DP instrument [70] with a 3 s resolution. Additionally, the IMF strength and component data with a resolution of 0.092 s provided by the MFI instrument [71] are used.

The identification of current sheets using the method proposed by Khabarova et al. [39] and the analysis of turbulence characteristics of the IMF with the building of the spectra are conducted for the same Wind data within the same time intervals, eliminating uncertainties related to comparing measurements from different spacecraft and instruments, as well as in statistical research results.

Figure 2 shows the temporal evolution of the IMF strength B and its components, along with the solar wind plasma parameters observed by Wind, namely, the solar wind bulk speed V_p , the proton density N_p , the proton temperature T_p , and the plasma beta representing the ratio of the proton thermal pressure to the magnetic pressure ($\beta = 2\mu_0 N_p k_B T_p / B^2$, where k_B is the Boltzmann constant) for the selected period of the passage of the merged ICME at the Earth’s orbit.

The solar wind types are marked by vertical lines indicating the arrival of the interplanetary shock wave, the approximate end of the classic ICME sheath and transition to the mixed sheath–magnetic cloud type (MC 1), and the beginning of the smoothly rotating magnetic field within the ICME magnetic obstacle.

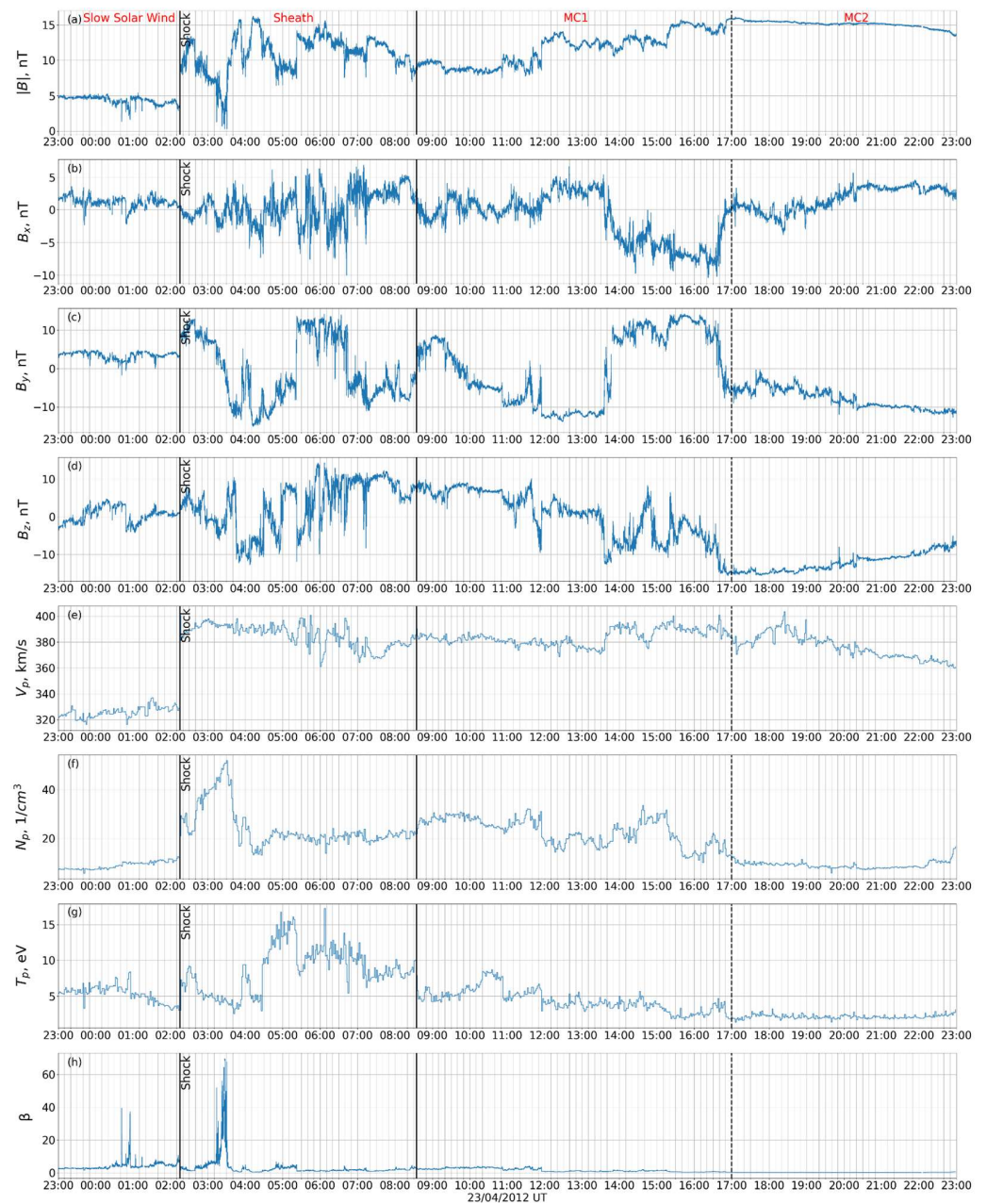


Figure 2. WIND observations of the IMF and plasma parameters associated with the ICME shown in Figure 1b. Temporal evolution of the IMF module and its components (a–d), plasma parameters (e–g) and plasma β parameter (h) in the interval from 22 April 2012 23:00 to 23 April 2012 23:00. Vertical lines from right to left show the ICME-driven shock, the end of the classic sheath region (bounded by two solid lines), and the beginning of the magnetic field variations associated with merged magnetic cloud–sheath region (magnetic cloud 1) formed as a result of CME–CME interaction shown in Figure 1b. Dashed line separates magnetic cloud 1 from magnetic cloud 2 with the more regularly rotating magnetic field.

To analyze the characteristics of turbulent fluctuations in the different types of solar wind shown in Figure 2, we build the frequency spectra of the parameter fluctuations for the corresponding time intervals. This approach is based on Taylor’s hypothesis, which is generally applicable to the solar wind [72]. According to this hypothesis, observed variations in temporal parameters can be interpreted as structures of varying spatial scales convected by the solar wind past the observation point. To compute the frequency spectra of fluctuations, we used the highest available resolution of the IMF data, up to ~ 10 Hz. For

the identification of current sheets, the IMF strength data were averaged to a one-second resolution. The proton density, temperature, and velocity vector data were interpolated to a one-second resolution as well.

The methodology for automatically determining characteristics of turbulent fluctuation spectra can be divided into several stages. First, we calculated the IMF fluctuation spectrum by constructing the spectra for each component of the IMF and summing them. Each spectrum was constructed using the fast Fourier transform (FFT) based on the original magnetic field component values with a time resolution of 0.092 s (the data were preprocessed into equidistant time series). The length of the analyzed interval was ~ 12.6 min, which corresponded to 8192 points, given the data resolution. This interval length was chosen because FFT is optimally performed with a point count that is a power of two. The study aims to examine the fluctuation spectra at both kinetic and MHD scales, making further reduction in the interval length unnecessary. Increasing the interval length is also undesirable because it increases the likelihood of capturing different structures within a single interval, complicating interpretation. Each subsequent analyzed interval was shifted by 1024 points (~ 1.5 min) with respect to the previous one, making a sliding window, to avoid losing information about fluctuations at the interval boundaries and to provide a more comprehensive view of the dynamics of turbulence characteristics.

The resulting spectrum was divided into three frequency ranges: the first corresponding approximately to MHD scales, the second to kinetic scales, and the third to the noise region. Initially, the boundaries of these regions were set manually: 1 Hz (as an initial approximation of the boundary between the MHD and kinetic scales) and 3 Hz (the approximate start of the noise region). The 1 Hz frequency was chosen as the preliminary boundary between the MHD and kinetic scales based on prior studies of solar wind turbulence spectra (see, for example, the review by Alexandrova et al. [40]). The 3 Hz frequency was chosen as the preliminary boundary for the noise region based on empirical experience. At the next step, using the piecewise linear approximation method [73], we found the slopes of the corresponding spectral regions. The positions of the boundaries between the MHD, kinetic, and noise parts of the spectrum were refined based on the approximation discussed above.

Figure 3 presents an example of the fluctuation spectrum (the blue curve) and the approximation obtained using the method described above (the orange lines). The spectrum clearly showed two regions where it could be approximated by linear dependencies with different slope indices. The intersection point of these linear approximations corresponded to a frequency of 0.66 Hz. In the first region, up to the breakpoint corresponding to MHD scales, the slope was $P_1 = -1.79$. In the frequency range from 0.66 to 2.96 Hz, corresponding to ion-kinetic scales, the slope was $P_2 = -2.63$. The spectrum shown in the figure is fairly typical for the solar wind (see, for example, the reviews by Alexandrova et al. [40], Bruno et al. [41]). Similar slope values were also generally observed for the solar wind plasma flow fluctuations [42]. At MHD scales, the calculated spectrum slope of -1.79 was steeper than the Kolmogorov scaling of $-5/3$, predicted for developed MHD turbulence in the solar wind [54], but it fell within the statistical range observed in various experiments [40]. At kinetic scales, the spectrum slope was -2.63 , close to the $-8/3$ slope predicted by several theoretical approaches (see, for example, [56,57]).

For the subsequent comparison of the spectral break frequency with key plasma frequencies, they were calculated as follows: the gyrofrequency $f_c = q_p B / (2\pi m_p)$ and the convection plasma frequencies determined by the thermal proton gyroradius $F_{\rho_i} = V_p / (2\pi \rho_{th})$. $\rho_{th} = V_{th} / \omega_c$ is the thermal proton gyroradius, V_{th} is the proton thermal velocity, and $\omega_c = qB / m_p$ is the cyclotron angular frequency. Additionally, the inertial proton length frequency $F_{\lambda_i} = V_p / (2\pi \lambda)$ was computed, where λ is the proton inertial length, defined as $\lambda = c / \omega_p$, ω_p being the proton plasma frequency. In Figure 3, the corresponding plasma frequencies are found to be $f_c = 0.13$ Hz, $F_{\rho_i} = 0.97$ Hz, and $F_{\lambda_i} = 1.31$ Hz. The spectral break of the IMF fluctuations located at 0.66 Hz is closest to the plasma frequency determined by the thermal proton gyroradius.

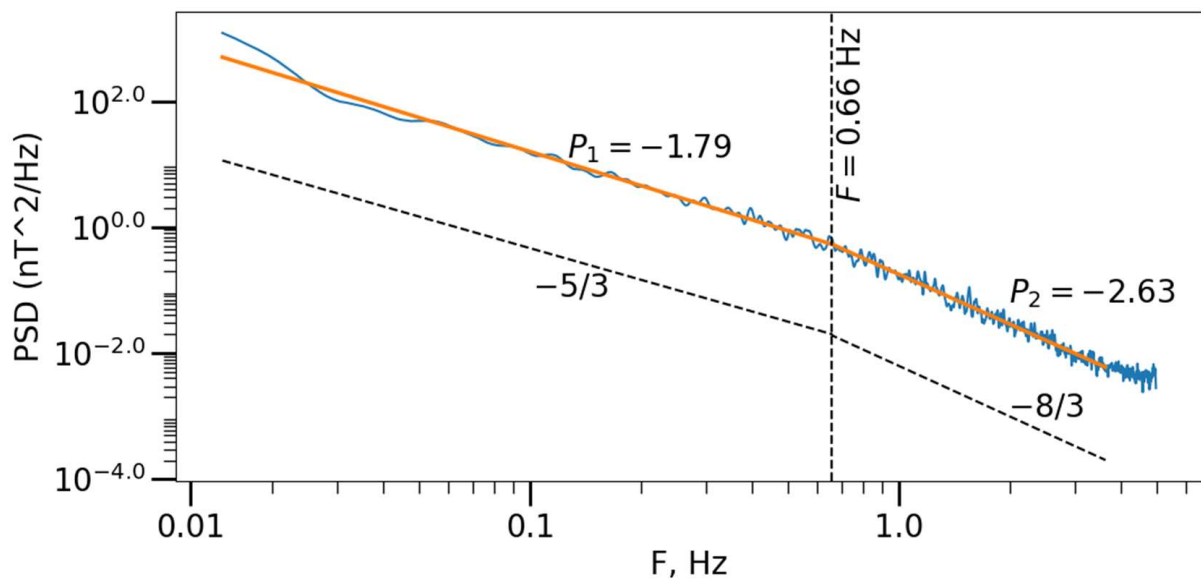


Figure 3. Example of the IMF fluctuation spectrum (blue curve) calculated for the interval 23 April 2012 04:45:04–04:57:38, along with the spectrum approximation in two frequency ranges (shown by straight orange lines): the slope P_1 at MHD scales and the slope P_2 at kinetic scales. Dashed lines indicate the slopes of $-5/3$ (for MHD scales) and $-8/3$ (for kinetic scales), corresponding to theoretical predictions.

Additionally, the angle between the IMF and solar wind speed vectors defining the primary direction of IMF fluctuations in the solar wind was calculated for all analyzed time intervals. This was carried out by finding the unit vectors corresponding to each pair of the IMF and velocity vectors and then computing the scalar product of these unit vectors. The angle itself was obtained by calculating the arccosine of the resulting scalar product.

To identify current sheets, the method proposed by Khabarova et al. [39] was utilized. This method detects characteristic features in plasma and IMF parameters when crossing a current sheet based on high time-resolution data. These features include (i) the sharp decrease in $|B|$ at current sheets, (ii) the decrease in V_A/V (where V_A is the Alfvén speed $V_A = B/(\mu_0 N_p m_p)^{-1/2}$, and μ_0 is the magnetic constant), and (iii) the increase in β . To identify these changes, derivatives of B , β , and V_A/V were calculated with a one-second cadence. Only peaks observed simultaneously in the derivatives of $|B|$ and any of the other two parameters indicated above were considered as pointing at current sheets. The threshold levels were selected by applying the condition of maximum correlation for the exceedance indicators of each parameter [39].

Figure 4 provides an example of the current sheet identification for the time interval 23 April 2012 04:45:04–04:57:38, which coincides with the interval shown in Figure 3. The current sheet identified at 04:49:44 was the most pronounced during this period. It is characterized by the sharp simultaneous drop in the derivatives of $|B|$ and V_A/V , along with a rise in the derivative of β . Most other current sheets during this period were identified by the simultaneous fulfillment of two out of three conditions indicated above. For instance, the current sheet at 04:46:02 was identified based on these two conditions alone. This was the only current sheet identified at 04:46, as other moments with drops in the derivatives of $|B|$ or V_A/V did not meet the simultaneity condition.

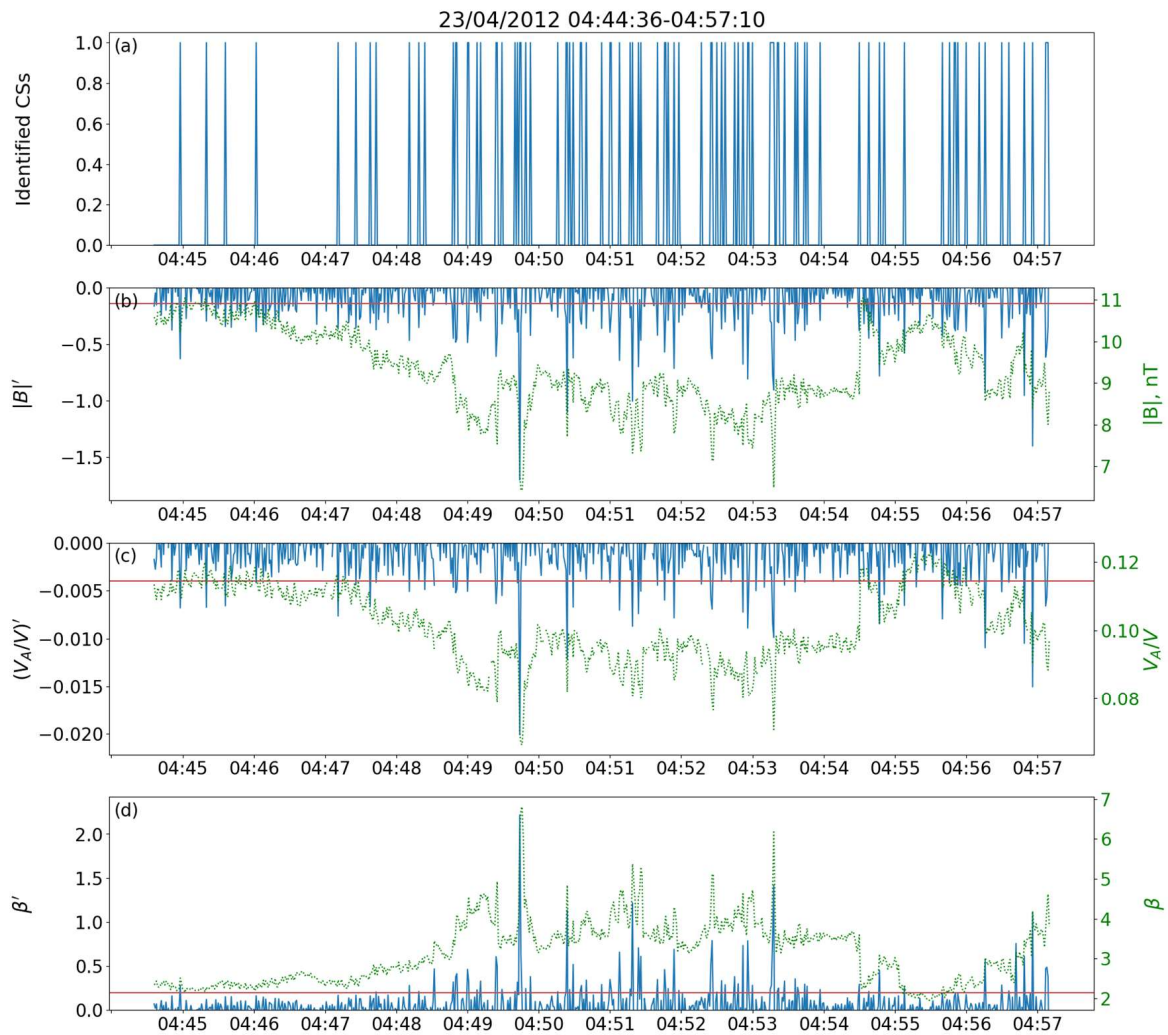


Figure 4. Example of applying the current sheet identification method to the interval 23 April 2012 04:45:04–04:57:38. From top to bottom: (a) location of the identified current sheets (1 means the presence of the current sheet); (b) derivative of the magnetic field magnitude; (c) derivative of the ratio of Alfvén speed to solar wind speed, and (d) derivative of the plasma β . Green dashed lines indicate the parameters used to calculate the derivatives, while the red lines represent the threshold levels for each parameter. Current sheets are identified by the simultaneous crossing of the threshold by the derivative of $|B|'$ and at least one of the other two parameters.

3. Results

We analyze and compare the characteristics of the turbulent cascade and the number of observed current sheets associated with the ICME shown in Figures 1b and 2 with a 24 h interval from 22 April 2012 23:00 to 23 April 2012 23:00. At the beginning of the interval, the quasi-stationary region of slow solar wind is observed, with the following average parameter values: $B \approx 4.37 \pm 0.005$ nT, $V_p \approx 328.26 \pm 0.06$ km/s, $n_p \approx 8.98 \pm 0.01$ cm⁻³, and $T_p \approx 5.28 \pm 0.01$ eV. As the ICME-driven shock arrives, the examined parameters sharply increase to the average values of $B \approx 10.98 \pm 0.02$ nT, $V_p \approx 385.28 \pm 0.06$ km/s, $n_p \approx 24.25 \pm 0.05$ cm⁻³, and $T_p \approx 8.61 \pm 0.02$ eV and become more volatile in the ICME sheath. After the classic sheath region ends, the plasma speed remains roughly at the same level and becomes less disturbed. The plasma density and the IMF strength gradually increase again, while the plasma temperature returns to a level similar to that before the interplanetary shock wave arrival.

Magnetic cloud regions 1 and 2 differ from other ICME parts in their strong and more regularly behaved magnetic fields. Note that Magnetic cloud 1 is a result of the

CME–CME interaction when the smaller ICME 2 overtakes larger ICME 1 and moves ahead until they merge and form a stream filled with a mixture of their structures. Taking into account an oblique crossing of the merged ICME at the Earth’s orbit (see Figure 1b), one may conclude that Magnetic cloud 2 belongs to the larger ICME 1, but Magnetic cloud 1 is a distorted and highly twisted flux rope of ICME 2. In the example considered in Figure 2, quasi-stationary behavior of the magnetic field is seen starting around 17:00, accompanied by stabilization of the temperature at a level lower than that in the calm solar wind preceding the ICME arrival. The density returns to calm solar wind levels, while the speed remains elevated and volatile. The average values observed in the interval from 17:00 to 23:00 are the following: $B \approx 15.09 \pm 0.003$ nT, $V_p \approx 381.06 \pm 0.07$ km/s, $n_p \approx 9.08 \pm 0.009$ cm⁻³, and $T_p \approx 2.09 \pm 0.002$ eV. Between the end of the classic turbulent sheath and the start of the more regular magnetic field region (from 08:35 to 17:00), noticeable variations in all parameters are observed, though not as intense as in the sheath, with average values of $|B| \approx 11.67 \pm 0.01$ nT, $V_p \approx 386.9 \pm 0.04$ km/s, $n_p \approx 22.82 \pm 0.03$ cm⁻³, and $T_p \approx 4.37 \pm 0.01$ eV. The averaged solar wind plasma and IMF parameters for the analyzed intervals are presented in Table 1.

Table 1. The IMF and plasma parameters observed within the intervals indicated in Figure 2.

Parameter	Interval			
	Slow SW	ICME Sheath	MC1	MC2
Density (1/cm ³)	8.98 ± 0.01	24.25 ± 0.05	22.82 ± 0.03	9.08 ± 0.01
Temperature (eV)	5.28 ± 0.01	8.61 ± 0.02	4.37 ± 0.01	2.09 ± 0.0
B (nT)	4.37 ± 0.0	10.98 ± 0.02	11.67 ± 0.01	15.09 ± 0.0
V _p (km/s)	328.26 ± 0.06	385.28 ± 0.06	386.9 ± 0.04	381.06 ± 0.07
f _c (Hz)	0.07 ± 0.0	0.17 ± 0.0	0.18 ± 0.0	0.23 ± 0.0
F _{pi} (Hz)	0.69 ± 0.0	1.68 ± 0.0	2.56 ± 0.01	4.35 ± 0.0
F _{λi} (Hz)	0.69 ± 0.0	1.31 ± 0.0	1.28 ± 0.0	0.8 ± 0.0
αBV	108.3 ± 0.1	91.7 ± 0.09	81.8 ± 0.09	94.29 ± 0.04
F _{break} (Hz)	0.28 ± 0.01	0.73 ± 0.02	0.78 ± 0.01	0.86 ± 0.02
P ₁	−1.68 ± 0.02	−1.76 ± 0.01	−1.68 ± 0.01	−1.59 ± 0.01
P ₂	−2.53 ± 0.02	−2.72 ± 0.03	−2.62 ± 0.02	−2.38 ± 0.02
cS _n	24.95 ± 1.4	56.11 ± 1.96	6.84 ± 0.29	0.03 ± 0.01

Figure 5 shows the time series of the following plasma parameters: the angle between the IMF and plasma speed vectors (a), plasma frequencies determined by the proton gyroradius (b), the proton inertial length (c), and the proton gyrofrequency (d), calculated for the time interval considered in Figure 2, as described in Section 2. Plasma frequencies increased by approximately 2–2.5 times after the ICME-driven shock arrives.

The average values of the key frequencies in the calm plasma are the following: $f_c = 0.07$ Hz, $F_{pi} = 0.69$ Hz, and $F_{λi} = 0.69$ Hz, and in the sheath, they increase to $f_c = 0.17$ Hz, $F_{pi} = 1.68$ Hz, and $F_{λi} = 1.31$ Hz. The average angle between B and V does not change significantly despite the ICME arrival (108° in the calm solar wind, and 91° in the sheath), although local variations in this angle can be substantial, especially in the sheath region. The sharp drop in the angle between B and V at 03:30 coincides with a decrease in gyrofrequency and plasma frequency determined by the proton gyroradius. However, this event has almost no effect on the plasma frequency determined by the proton inertial length. The averaged calculated plasma parameters are also presented in Table 1.

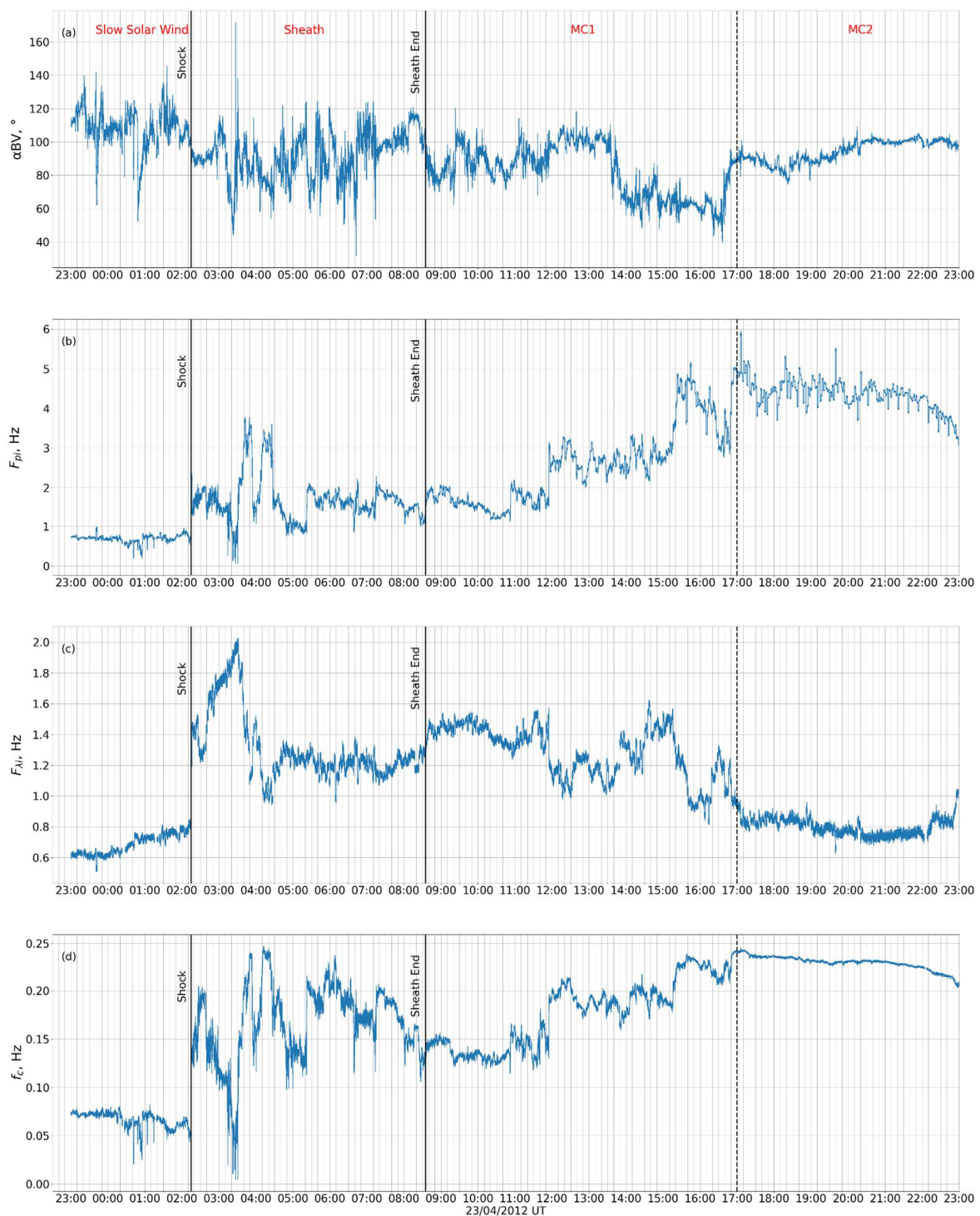


Figure 5. Variations in the angle between the magnetic field and the solar wind speed and key frequencies observed within the time interval shown in Figure 2. From top to bottom: temporal evolution of the angle between the IMF and solar wind velocity vectors (a), characteristic frequencies determined by proton gyroradius (b), inertial length (c), and the proton gyrofrequency (d).

The upper panel of Figure 6 shows the temporal evolution of the number of current sheets (cs_n) calculated over 12-min intervals with a 95 s step, consistent with the step used for spectral calculations. The panel below it shows the temporal evolution of the IMF fluctuation spectra characteristics, including the slope of the spectra in the MHD (P_1) and kinetic (P_2) scales, as well as the break frequency between them. Dashed lines on the

corresponding panels indicate a slope of $-5/3$, characteristic of Kolmogorov turbulence in the MHD range, and slopes of $-7/3$ and $-8/3$, predicted by various models for kinetic Alfvén turbulence in the kinetic range, as discussed in the Introduction. In the quiet solar wind, the average values observed are $F_{\text{Break}} = 0.28 \pm 0.01$ Hz, $P_1 = -1.68 \pm 0.02$, $P_2 = -2.53 \pm 0.02$, and $c_{S_n} = 24.95 \pm 1.0$.

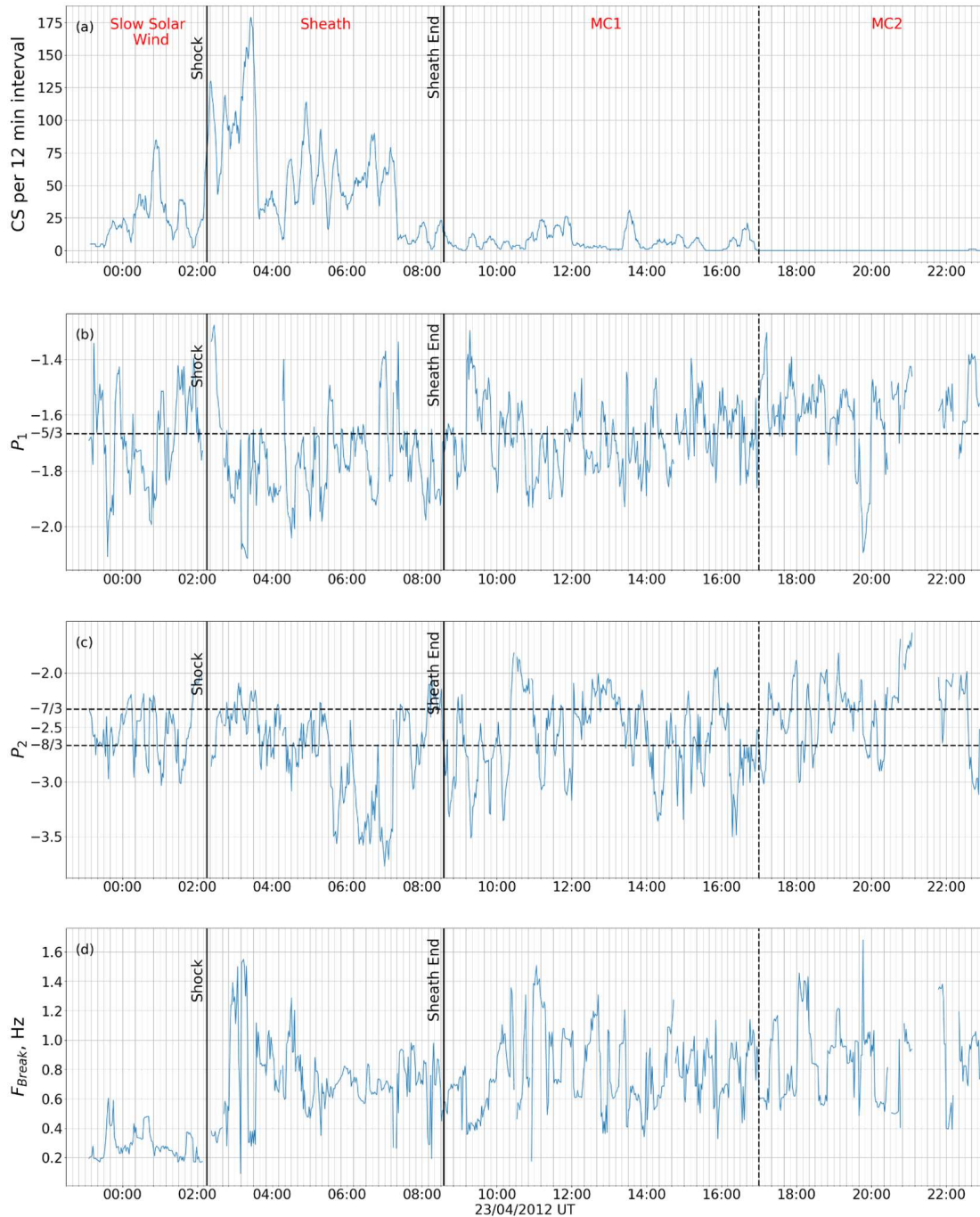


Figure 6. Current sheet rate and characteristics of turbulent IMF fluctuations found within the time interval shown in Figure 2. Vertical lines correspond to explanation at Figure 2. Number of current sheets over 12 min intervals (c_{S_n}) (a), the slope of the IMF fluctuation spectrum in the MHD range (P_1) with a dashed line indicating the $-5/3$ slope (b), the slope of the IMF fluctuation spectrum in the kinetic range (P_2) with dashed lines indicating the $-7/3$ and $-8/3$ slopes (c), and the break frequency between the MHD and kinetic ranges of the fluctuation spectrum (F_{Break}) (d).

Following the arrival of the shock, the number of current sheets sharply increases to an average value of $cs_n = 56.11 \pm 2.0$ in the ICME sheath. After peaking at 03:28, the number of current sheets begins to decline, which continues until the beginning of the Magnetic cloud 2 region (15 h after the shock arrival). This behavior is consistent with the analysis of current sheet counts around ICME events using the superposed epoch method [39]. Additionally, one may notice a 2.5-fold increase in the break frequency and a steepening of the spectral slopes P_1 and P_2 (average values: $F_{\text{Break}} = 0.73 \pm 0.02$ Hz, $P_1 = -1.76 \pm 0.01$, $P_2 = -2.72 \pm 0.03$). In some intervals, the spectral slope values at kinetic scales reach -3.5 , while the median value for the interval is -2.62 . The steepening of the slopes in the kinetic region of the spectrum aligns with the statistical studies of fluctuation spectra in the ICME sheaths presented in [60].

In the period between the end of the plasma compression region and the beginning of the Magnetic cloud 1–2 region, the number of current sheets decreases noticeably compared to the sheath, but does not reach the low values observed within the magnetic cloud region. The break frequency increases by approximately 5%, and the spectral slope values return to levels similar to those in the quiet solar wind. The average values for this period are the following: $F_{\text{Break}} = 0.78 \pm 0.01$ Hz, $P_1 = -1.68 \pm 0.01$, $P_2 = -2.62 \pm 0.02$, and $cs_n = 6.11 \pm 0.3$. Upon entering Magnetic cloud 2, the number of current sheets approaches zero, the break frequency continues to increase, and the spectral slopes become flatter compared to the quiet solar wind. The average values in the magnetic cloud region are the following: $F_{\text{Break}} = 0.86 \pm 0.02$ Hz, $P_1 = -1.59 \pm 0.01$, $P_2 = -2.38 \pm 0.02$, $cs_n = 0.03 \pm 0.01$. Meanwhile, P_1 and P_2 values become more volatile here, which might be attributed to the low level of magnetic field fluctuations in this region and the associated uncertainties in the approximation of fluctuation spectra.

In the sheath region before the magnetic cloud (particularly at its onset), there is a sharp increase in the number of current sheets, with several pronounced peaks visible at 02:22, 02:45, and 03:28. A cluster of elevated current sheet activity can be identified between 02:00 and 03:30, with an average of approximately 95 current sheets per 12.6 min interval. A correlation is observed between the increase in current sheets during this interval and the steepening of the P_1 slope in the MHD range of the IMF fluctuation spectrum (average P_1 value = -1.74), although the slope values vary significantly during this period. Conversely, the spectrum slope in the kinetic range P_2 becomes flatter (average P_2 value = -2.36). Notably, in the latter part of the ICME sheath, where the number of current sheets decreases, the P_2 slopes steepen, reaching values as low as -3.5 . The break frequency of the spectrum fluctuates widely, ranging from 0.2 to 1.5 Hz.

A detailed comparison of Figures 5 and 6 reveals that, at the peak of identified current sheets (03:28, with 175 sheets over a 12.6-min interval), there is a sharp spike in the angle between the IMF direction and the speed to $\sim 160^\circ$, accompanied by the steepening of the P_1 slope to -2 and a sudden drop in the break frequency to ~ 0.4 Hz. However, no significant changes in the P_2 slope are observed compared to previous points.

Figure 7 shows the IMF fluctuation spectra for intervals associated with the increase in current sheets around $\sim 3:28$. It is evident that all presented spectra, compared to typical ones, exhibit steeper slopes in the MHD range and flatter slopes in the kinetic range. The difference between the slopes becomes minimal, meaning the spectral break nearly disappears. In these cases, the angle between the IMF direction and the velocity shows no significant deviations from their average values.

Figure 8 illustrates the temporal evolution of the current sheet number and break frequency, marking instances of sharp increases in cs_n during the examined interval. The cs_n increase is accompanied by the drop in the break frequency, though statistical confirmation of this relationship has yet to be achieved.

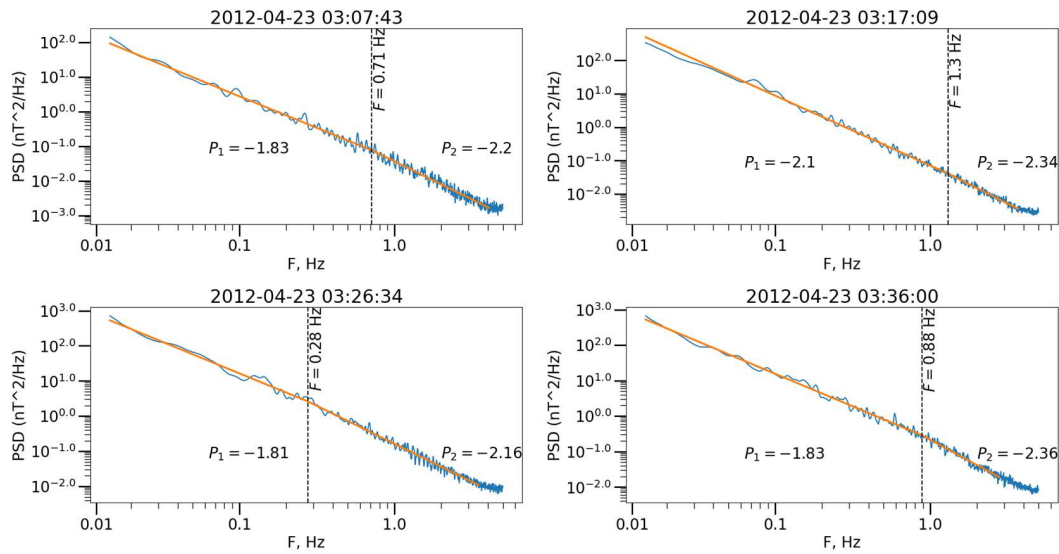


Figure 7. Spectra of the IMF fluctuations (blue curves) in the vicinity of the cs_n peak observed 23 April 2012, t 03:28. Orange lines present the spectra approximations.

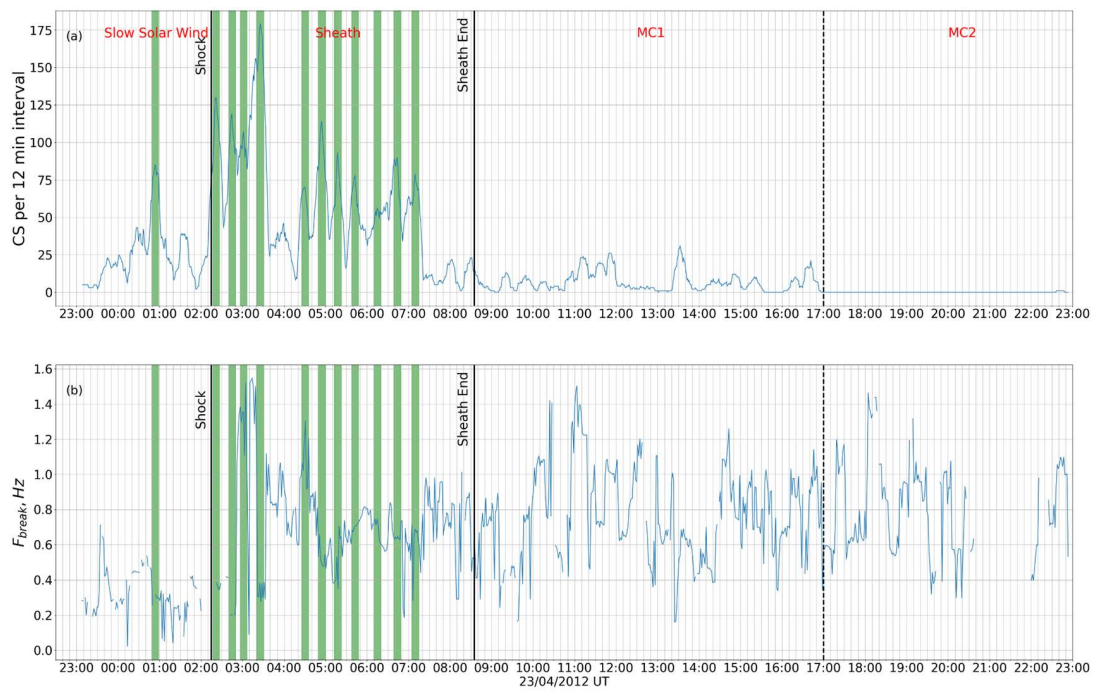


Figure 8. Comparison of the current sheet rate and the break frequency within the time interval shown in Figure 2. Vertical lines indicate the edges of the ICME parts shown in Figure 2. Temporal evolution of the number of current sheets in 12 min intervals (a) and break frequency between the MHD and kinetic ranges (b). Green stripes indicate moments when the number of current sheets exceeds 50.

To show the most often occurring patterns in the behavior of the spectra characteristics, we compare several peaks in the number of current sheets seen in the upper panel of Figure 6 with P_1 , P_2 , F_{break} , and T_p . As mentioned above, the connection between current sheets, turbulence, magnetic reconnection, and heating has been highlighted in numerous statistical studies. However, it remains unclear whether temperature increases at current sheets due to the reconnection process or if current sheets simply form at points where the temperature is already at its peak. Therefore, we include T_p in the analysis as well.

Figure 9 depicts intervals with peaks in cs_n observed within the quiet solar wind period and all ICME parts except for MC2, where there are no noteworthy cs_n peaks. From top to bottom, the two panels show cs_n , the slope of the IMF fluctuation spectrum in the MHD range, the slope of the IMF fluctuation spectrum in the kinetic range, the break frequency between the MHD and kinetic ranges, and the proton temperature. cs_n and T_p are normalized to their mean values within the corresponding intervals. P_1 is normalized to the expected slope $-5/3$, and P_2 is normalized to the expected slope $-8/3$.

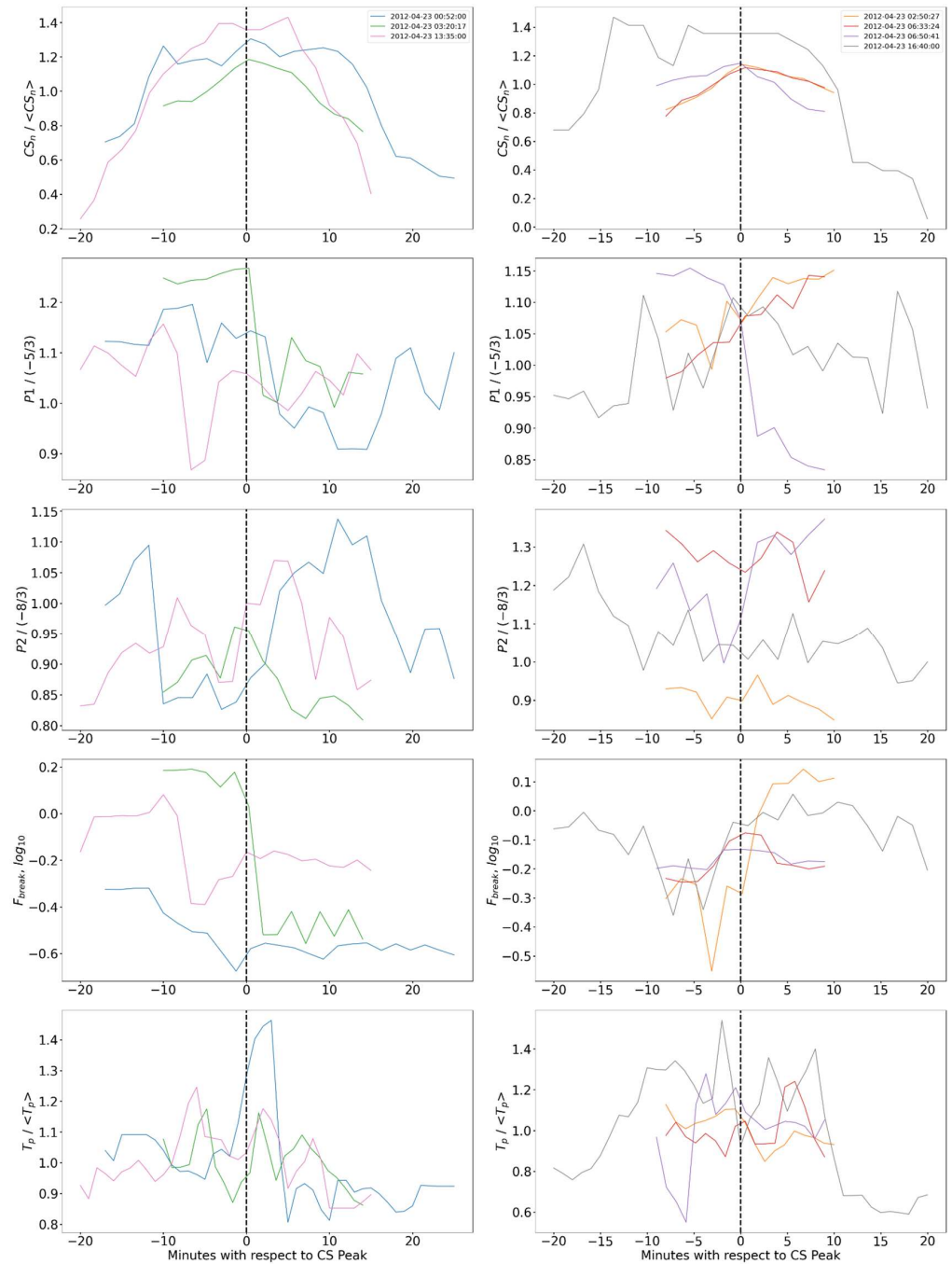


Figure 9. Typical variations in spectra properties and proton temperature associated with peaks in the number of current sheets. From top to bottom: cs_n , P_1 , P_2 , F_{break} , and T_p . All parameters, except for F_{break} , are normalized as described in the text. Vertical dashed lines show the current sheet number peak for each time interval indicated in the legend.

The peaks in cs_n , despite varying in width, have a distinguishable relationship with F_{break} , which usually peaks in the vicinity of the cs_n , with sharp changes occurring within minutes before or after. These changes can be in either direction—from larger values to smaller (left panel) or smaller to larger (right panel). While P_1 and P_2 values also shift rapidly during these intervals, their changes do not align with the direction of F_{break} fluctuations. The temperature rarely peaks exactly at the cs_n maximum. Very often, there are two or more distinctive peaks around the cs_n peak, and the general trend of the temperature increase associated with the increasing number of current sheets is evident. This illustrates the fact that the link between the solar wind heating and current sheets in the solar wind as well as the spectra properties and current sheets still remains at the statistical level or requires far more case studies.

We analyze the behavior T_p at current sheets observed in different types of solar wind plasma by building histograms of the temperature distributions in the undisturbed solar wind, ICME sheath, and MC 1. The number of current sheets in MC 2 does not allow us to perform any kind of statistical analysis. The histograms shown in Figure 10 are built for values at current sheets and in the solar wind without current sheets. The MC 2 interval does not contain enough current sheets to allow the corresponding histogram to be statistically significant. The top histograms display the temperature distributions for the seconds during which current sheets are detected (blue) and for the seconds without current sheets (red), while the bottom histograms show the percentage of seconds with detected current sheets per the temperature bin, illustrating the impact of current sheets on the temperature distributions. Proton temperatures at current sheets are consistently higher than those away from current sheets. For instance, in the 8–10 eV bin, which contains the highest values of the temperature observed during the undisturbed period, approximately 20% of seconds are associated with current sheets, even though current sheets represent only 3.3% of the total time frame (375 current sheets out of 11,333 s). The median temperature at the current sheets is about 7% higher than that away from current sheets. In the ICME sheath (middle panels), current sheets form two populations—with the lowest and highest temperatures. The distribution reveals two distinct peaks: one at 4–6 eV and the other at 10–12 eV. Around 12% of the 4–6 eV bin and over 7% of bins within the 10–18 eV range consist of seconds with detected current sheets, indicating that they significantly contribute to the higher temperatures while also being prominent in colder plasma. In total, 1793 current sheets are observed over 20,998 s, accounting for approximately 8.5% of the ICME sheath period. During the MC 1 period (rightmost panels), there is also a shift to higher temperatures associated with current sheets similar to that seen in the undisturbed solar wind, although the number of current sheets is rather low in this interval (less than 1%, or 286 out of 30,014 s). No bin contains more than 2% of seconds with detected current sheets, with the peak occurring in the 6–8 eV bin.

Therefore, the occurrence of current sheets is statistically associated with the maximal temperatures observed in all types of solar wind under study. Two populations of current sheets (namely, cold and hot current sheets) observed in the turbulent ICME sheath with the largest number of these structures may be related to the presence or absence of the ongoing magnetic reconnection at the particular current sheets. This phenomenon may also be explained by the co-existence of current sheets of different origins, for example, thin and short-scale structures created by turbulence and large-scale quasi-stable current sheets formed downstream of the ICME-drive shock at early stages of its propagation. Both ideas should be checked in the future with larger statistical material and detailed studies of the properties of current sheets.

Figure 11 illustrates the statistical dependencies between cs_n and the angle between \mathbf{B} and \mathbf{V} , characteristic plasma frequencies, and parameters of the IMF fluctuation spectra. The details of the statistical relationship between the current sheet number and other important parameters, namely, $|V|$, $|B|$, N_p , β , T_p , f_c , $F_{\lambda i}$, and F_{pi} , are given in Appendix A. Different colors signify values observed in the four intervals indicated in Figure 2: the quiet slow solar wind (green), the ICME sheath (red), MC1 (blue), and MC 2 (orange).

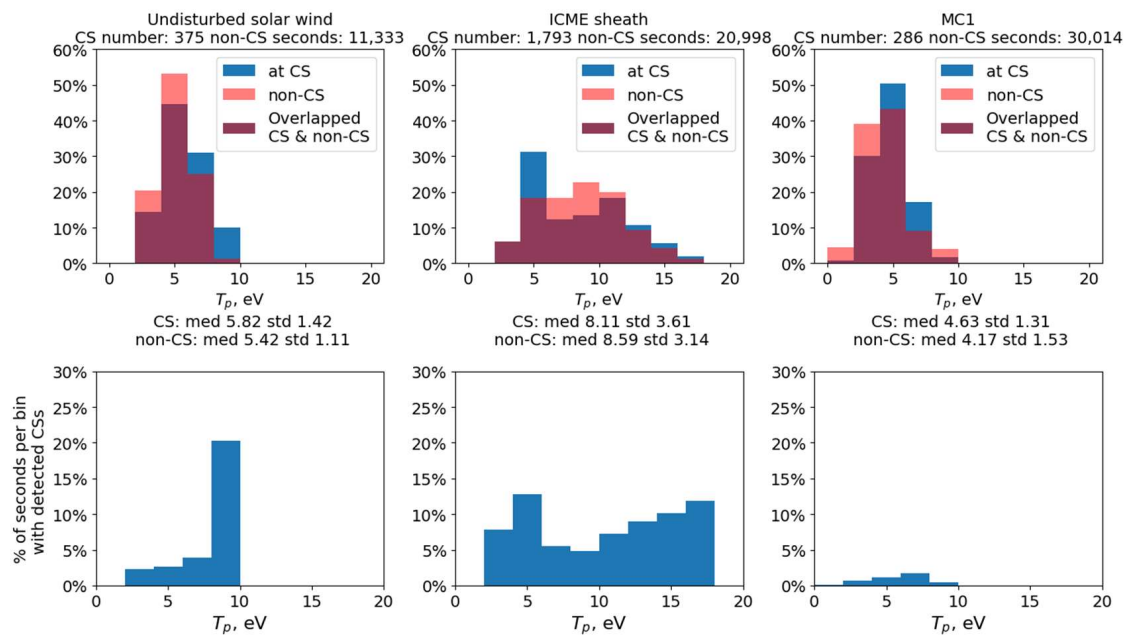


Figure 10. Comparison of the proton temperature (T_p) at and away from current sheets across different types of solar wind. Top panels display the plasma temperature distribution, while the bottom panels illustrate the percentage of seconds with detected current sheets per temperature bin. From left to right: undisturbed solar wind, ICME sheath, and MC 1.

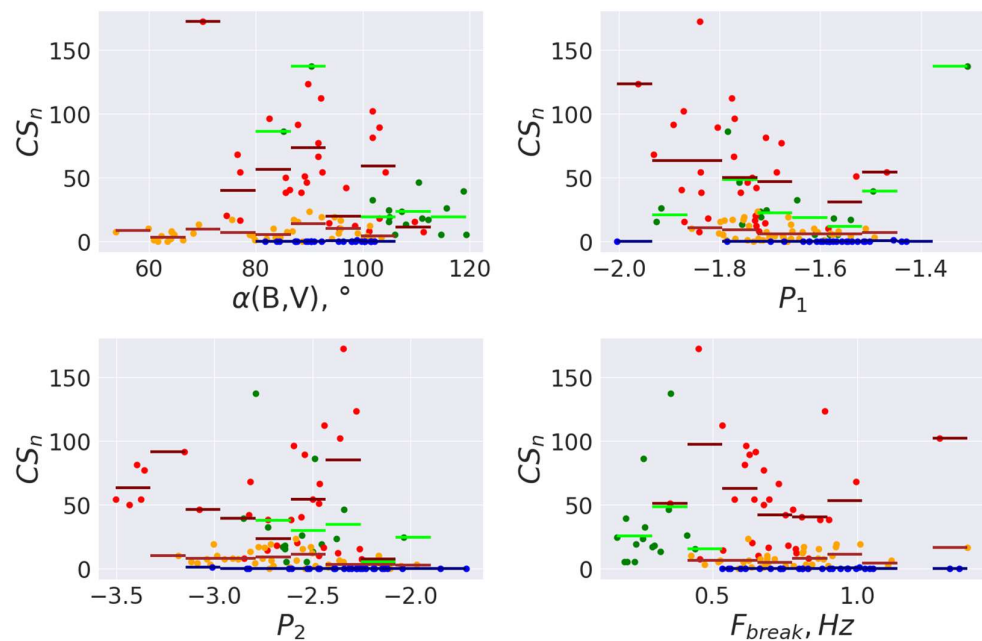


Figure 11. Relationship between the number of current sheets in 12.6 min intervals and the average values of parameters characterizing spectra of IMF variations. Left to right, top to bottom: angle between the B and V vectors, slope of the fluctuation spectrum in the MHD range, slope of the fluctuation spectrum in the kinetic range, and break frequency between the MHD and kinetic ranges of the fluctuation spectrum. Color of the points indicates the type of solar wind: green reflects slow and quiet solar wind, red is for the ICME sheath, blue indicates MC 2, and orange indicates MC 1. Horizontal lines represent the average number of current sheets for the corresponding parameter value range.

No relationship is observed between the number of current sheets and the parameters in the magnetic cloud regions, where cs_n is low. However, for the sheath region, clear inverse correlations of cs_n with $|B|$ and the angle between the \mathbf{B} and \mathbf{V} vectors are evident. Similar correlations are observed for the angle between \mathbf{B} and \mathbf{V} in the undisturbed solar wind region before the ICME arrival.

In the ICME sheath, the following additional dependencies are found between cs_n and characteristic plasma frequencies: a direct correlation with the frequency associated with the proton inertial length and inverse correlations with the gyrofrequency and the frequency associated with the proton gyroradius. These correlations are likely related to dependencies on solar wind parameters.

For the ICME sheath, a clear statistical relationship is identified between the number of current sheets and the spectral break frequency—the growth of current sheet number is accompanied by a significant decrease of spectral break frequency. For other types of solar wind, such a dependence is not obvious. Meanwhile, there is no clear connection between cs_n and the spectral slopes of magnetic field fluctuations in either the MHD or kinetic ranges in any of the solar wind types. This is possibly related to the fact that there is a rapid restructuring of the spectrum, and the slopes are not stable and vary greatly.

Additionally, it can be noticed that the cs_n maximum is associated with the extreme slope values in the MHD range (-2 to -2.1 and -1.3 to -1.4 , respectively). Meanwhile, this result is not statistically significant due to the limited number of such events.

4. Discussion

This study is the first step to examine the relationships between the number of current sheets and the characteristics of the IMF fluctuation spectra in the solar wind. Current sheets were identified at 1 AU using an automated method (<https://csdb.izmiran.ru/>, accessed on 1 November 2024), enabling both case studies and statistical analysis of the links between the number of current sheets and the key parameters describing solar wind conditions and turbulence over a 24-h interval with different types of the solar wind.

In the slow, undisturbed solar wind, a moderate number of current sheets is observed, while the ICME sheath exhibited the highest number of current sheets compared to both intervals within the magnetic cloud and in the quiet solar wind, ranging from dozens to hundreds, which aligns with prior statistical studies [39]. This feature indicates that current sheets in the sheath are local structures formed within the turbulent and compressed solar wind plasma downstream of the interplanetary shock. In the magnetic cloud highly fragmented owing to the merging of two CMEs, where intense magnetic field fluctuations are observed, the number of current sheets decreased. In the classic magnetic cloud with the regularly rotating magnetic field, the number of current sheets dropped to a very low value, even lower than those in the undisturbed solar wind.

We find that in the slow undisturbed solar wind, spectra characteristics are close to model predictions. In the ICME sheath, the dynamics of turbulent cascades exhibit complex behavior, particularly in the narrow region downstream of the ICME-driven shock, where current sheets are most abundant. The number of current sheets increased in the ICME sheath sharply, and the slopes of spectra in the kinetic range generally become steeper, which is in agreement with the results of our previous works [39,60]. In the fragmented magnetic cloud, the characteristics of the fluctuation spectra are similar to those in the quiet solar wind. In the classic magnetic cloud, the spectra become the flattest in both scales, which reflects a significant decrease in magnetic field fluctuations in this region [74].

Prior studies have shown that the ICME sheath can be characterized by significant steepening of the fluctuation spectra at the kinetic scale [60]. A relation between the turbulent cascade properties and current sheets has previously been studied by different authors using observations in the magnetosheath [26,38] and in the solar wind [75,76]. Particularly, Greco et al. [75] employed the Cluster data to show that the turbulent cascade naturally leads to the formation of current sheets at various scales, down to the proton skin layer. At smaller scales, current sheet fragmentation processes occur, which can lead to the

formation of Harris-type layers at scales down to the electron skin layer [18]. Therefore, the results of prior statistical and case studies allowed assuming a relationship between the occurrence of current sheets and the steepening of IMF fluctuation spectra in the kinetic range, but no direct comparisons between the number of current sheets and turbulence state have been made.

Case studies show that spectral characteristics can change dramatically at current sheets, and significant perturbations of spectra of turbulent fluctuations occur in the vicinity of the current sheet number peak. Peaks in the number of current sheets are typically observed within 20–40 min intervals. Such a clustering of current sheets is a well-known phenomenon, driven by the ability of reconnecting or unstable current sheets to generate secondary coherent structures in their vicinity [17,18,39].

As noted in the Introduction, the number of current sheets is governed by the combined kinetic and thermal energy density, which is indirectly linked with the intensity of dynamic processes occurring at current sheets, such as magnetic reconnection and instabilities. Despite knowing that, the relationship between the number of current sheets and spectral characteristics under different plasma and IMF conditions has not been previously analyzed. Our case studies show that the slope of the spectra of IMF fluctuations generally becomes steeper at the MHD scale, together with the slopes at the kinetic scale that become flatter in the vicinity of the cs_n maximum. The two branches of the spectra may even merge into one, and the break can disappear. Further beyond, a significant steepening of the spectra is observed, indicating that the presence of current sheets impacts the turbulent cascade over a much larger area than expected since this effect extends well beyond the peaks in the number of current sheets, reflecting the central region of the most active turbulent reconnection.

The sharp rise in small-scale current sheet number and the changes in the fluctuation spectrum, including its steepening at the kinetic scale, may reflect different aspects of the turbulence cascade development within the ICME sheath constrained by two strong discontinuities (the ICME-driven shock and the strong current sheet). The corresponding dynamic processes may be similar to those forming the turbulence spectra in the magnetosheath bounded by the Earth's bow shock and the magnetopause [44] and stream/corotating interaction regions [60,77–80].

Our statistical analysis reveals a clear correlation between the break frequency and the number of current sheets, while the relationship between spectral slopes and current sheet occurrence is less defined, making it challenging to establish a consistent connection. This uncertainty arises because, in the broader vicinity of the cs_n peak (on the scale of tens of minutes), the behavior of spectral parameters fluctuates significantly, but follows no consistent pattern. For instance, P_1 and P_2 may shift from lower to higher values in some cases, and from higher to lower in others. As a result, statistically, no clear links are found, but future case-by-case analysis may help clarify such relationships more effectively.

This may indicate that the characteristics examined depend not only on the type of large-scale solar wind flow, but also on its structure at smaller scales. Such a scenario is also characteristic of turbulent magnetic reconnection (e.g., [17,19,25]). This type of reconnection suggests that the current sheet is not merely a planar discontinuity separating large-scale magnetic fields with different directions. Instead, it has an internal structure composed of smaller-scale current layers and undergoes magnetic reconnection at multiple locations within it. Consequently, the primary current sheet generates secondary current sheets, flux ropes, and waves in its vicinity. Numerous secondary current sheets are small-scale and short-lived in comparison with the main current sheet that remains relatively long-lived and elongated. In spectral terms, this implies that plasma turbulence is most intense not directly at the strong current sheets, but in the surrounding regions.

In the context of solar wind heating, our findings confirm a statistical association between the presence of current sheets and increased temperatures. However, detailed analysis does not reveal clear temperature peaks corresponding directly to peaks in the number of current sheets. Instead, the temperature increase is observed on larger scales sur-

rounding the current sheets, aligning with the idea that current sheets reconnecting within turbulent regimes act as heating sources extending to MHD scales. It is also important to consider that current sheets may form more intensively in hot plasma due to various instabilities linked to local temperature increases (as discussed in [39]). Further research is needed to explore the relationship between current sheets, turbulence, and solar wind heating, taking these factors into account.

This research is useful for advancing our understanding of how current sheets influence turbulent fluctuation spectra and dissipation processes in the solar wind. Expanding the analysis to a larger dataset of ICMEs and other types of flows in the solar wind could provide clearer insights into the patterns observed in this work, particularly regarding the relationship between current sheets and the characteristics of turbulent plasma in stream interaction regions sharing similar characteristics with the ICME sheath. A detailed investigation into the connection between current sheet properties and local plasma temperature is essential to fully grasp the dependencies found in this study.

5. Conclusions

The study is aimed at comparing the properties of the turbulent cascade and the current sheet occurrence in different types of solar wind at 1 AU. The main results can be summarized as follows:

1. A case study analysis shows the link between the increase in the number of current sheets and the abrupt changes in spectral slopes and break frequencies.
2. A statistical analysis shows the anticorrelation of the spectral break frequency and the number of current sheets in all analyzed types of solar wind.
3. The abundance of small-scale current sheets inside the ICME sheath leads to changes in plasma dynamics and results in restructuring of the turbulent cascade. This fact indicates a significant impact of thin current sheets on dissipation processes in large-scale regions of compressed and turbulent plasma.
4. The relationship between plasma heating and the formation of current sheets is evident across various types of the solar wind. In both the slow, undisturbed solar wind and the disturbed magnetic cloud, where current sheets are relatively sparse, current sheets are predominantly found in the hottest plasma. In contrast, the turbulent ICME sheath, which has the highest number of current sheets, reveals two distinct populations of current sheets, occurring in both the hottest and coldest plasma within the region. This phenomenon may be linked to the coexistence of reconnecting and non-reconnecting current sheets or current sheets of different origins and requires further investigations.

Author Contributions: Conceptualization, M.O.R. and O.K.; methodology, T.V.T. and L.S.R.; software, T.V.T.; validation, O.K. and Y.I.Y.; formal analysis, T.V.T., M.O.R., and O.K.; investigation, T.V.T., M.O.R., and O.K.; data curation, M.O.R. and O.K.; writing—original draft preparation, O.K., M.O.R., T.V.T., and A.A.K.; writing—review and editing, O.K.; visualization, T.V.T.; supervision, Y.I.Y.; project administration, Y.I.Y. All authors have read and agreed to the published version of the manuscript.

Funding: The study is supported by the Russian Science Foundation grant no. 22-12-00227, <https://rscf.ru/en/project/22-12-00227/>.

Data Availability Statement: Wind spacecraft data were obtained using the NASA/GSFC Space Physics Data Coordinated Data Analysis Web (CDAWeb) facilities https://cdaweb.gsfc.nasa.gov/istp_public/ (accessed on 1 November 2024). We thank the Center for Astrophysics and Space Sciences (CASS) at the University of California, San Diego (UCSD), US, and the Institute for Space-Earth Environmental Research (ISEE), Nagoya University, Japan, for providing the solar wind density reconstructions used in the study (<https://ips.ucsd.edu/>).

Acknowledgments: Olga Khabarova's research was carried out as part of the activity of the Space Weather Center of Tel Aviv University (<https://www.spaceweather.sites.tau.ac.il>, accessed on 1 November 2024) with the assistance of the Center for Absorption in Science, Ministry of Immigration and Absorption, State of Israel.

Conflicts of Interest: The authors declare no conflicts of interest.

Appendix A

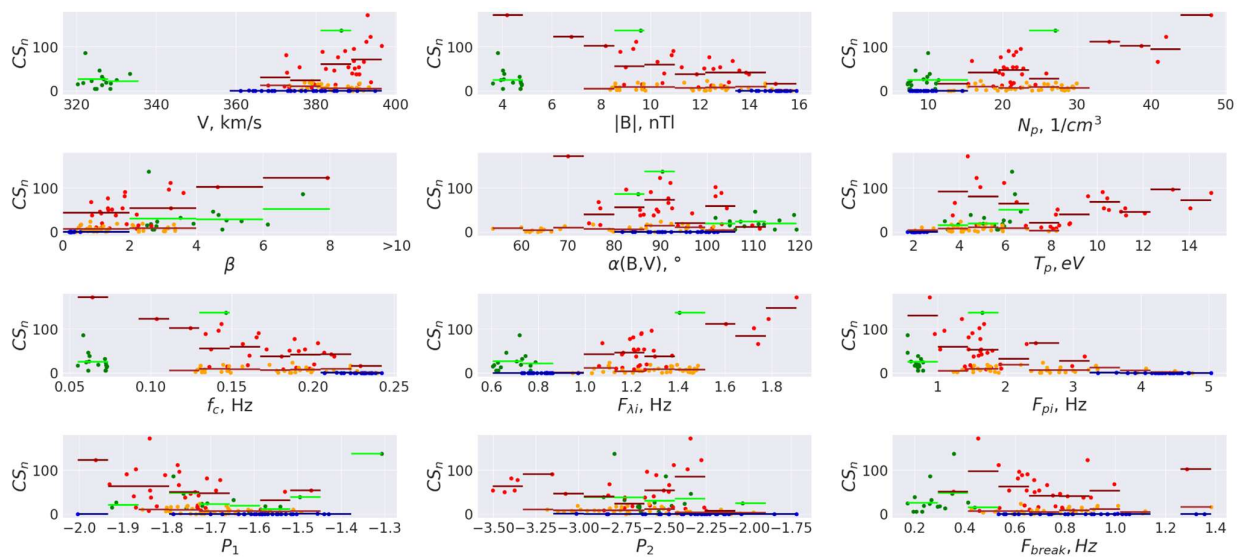


Figure A1. Relationship between the number of current sheets in 12.6 min intervals and the averaged values of various parameters (from left to right, top to bottom): V , magnetic field magnitude (B), proton concentration (N_p), β , angle between the B and V vectors, proton temperature (T_p), gyrofrequency (f_c), frequencies determined by the inertial length (F_{λ_i}) and proton gyroradius (F_{p_i}), the slope of the fluctuation spectrum on MHD scales (P_1), the slope of the fluctuation spectrum on kinetic scales (P_2), and the break frequency between the MHD and kinetic regions of the fluctuation spectrum (F_{break}). The color of the point indicates the type of solar wind in which the interval is located: green—quiet solar wind, red—ICME sheath, blue—MC 1, orange—MC 2. Horizontal bars indicate the average number of current sheets for the range of values of the corresponding parameter.

References

- Richardson, J.D.; Smith, C.W. The radial temperature profile of the solar wind. *Geophys. Res. Lett.* **2003**, *30*, 1206. [\[CrossRef\]](#)
- Elliott, H.A.; Henney, C.J.; McComas, D.J.; Smith, C.W.; Vasquez, B.J. Temporal and radial variation of the solar wind temperature-speed relationship. *J. Geophys. Res. Space Phys.* **2012**, *117*, A09102. [\[CrossRef\]](#)
- Kislov, R.A.; Khabarova, O.V.; Malova, H.V. A new stationary analytical model of the heliospheric current sheet and the plasma sheet. *J. Geophys. Res. Space Phys.* **2015**, *120*, 8210–8228. [\[CrossRef\]](#)
- Venzmer, M.S.; Bothmer, V. Solar-wind predictions for the Parker Solar Probe orbit. Near-Sun extrapolations derived from an empirical solar-wind model based on Helios and OMNI observations. *Astron. Astrophys.* **2018**, *611*, A36. [\[CrossRef\]](#)
- Matthaeus, W.H.; Zank, G.P.; Smith, C.W.; Oughton, S. Turbulence, Spatial Transport, and Heating of the Solar Wind. *Phys. Rev. Lett.* **1999**, *82*, 3444–3447. [\[CrossRef\]](#)
- Zank, G.P.; Matthaeus, W.H.; Smith, C.W.; Oughton, S. Heating of the solar wind beyond 1 AU by turbulent dissipation. *AIP Conf. Proc.* **1999**, *471*, 523–526. [\[CrossRef\]](#)
- Breech, B.; Matthaeus, W.H.; Cranmer, S.R.; Kasper, J.C.; Oughton, S. Electron and proton heating by solar wind turbulence. *J. Geophys. Res. Space Phys.* **2009**, *114*, A09103. [\[CrossRef\]](#)
- Wan, M.; Matthaeus, W.H.; Roytershteyn, V.; Karimabadi, H.; Parashar, T.; Wu, P.; Shay, M. Intermittent dissipation and heating in 3D kinetic plasma turbulence. *Phys. Rev. Lett.* **2015**, *114*, 175002. [\[CrossRef\]](#)
- Adhikari, L.; Zank, G.P.; Hunana, P.; Shiota, D.; Bruno, R.; Hu, Q.; Telloni, D. II. Transport of nearly incompressible magnetohydrodynamic turbulence from 1 to 75 au. *Astrophys. J.* **2017**, *841*, 85. [\[CrossRef\]](#)
- Chalov, S.V.; Alexashov, D.B.; Fahr, H.-J. Heating of the solar wind in the outer heliosphere. *Astrophys. Space Sci. Trans.* **2006**, *2*, 19–25. [\[CrossRef\]](#)
- Squire, J.; Meyrand, R.; Kunz, M.W.; Arzamasskiy, L.; Schekochihin, A.A.; Quataert, E. High-frequency heating of the solar wind triggered by low-frequency turbulence. *Nat. Astron.* **2022**, *6*, 715–723. [\[CrossRef\]](#)
- Kellogg, P.J.; Mozer, F.S.; Moncuquet, M.; Malaspina, D.M.; Halekas, J.; Bale, S.D.; Goetz, K. Heating and Acceleration of the Solar Wind by Ion Acoustic Waves—Parker Solar Probe. *Astrophys. J.* **2024**, *964*, 68. [\[CrossRef\]](#)

13. Wang, X.; Tu, C.; He, J.; Marsch, E.; Wang, L. On Intermittent Turbulence Heating of the Solar Wind: Differences Between Tangential and Rotational Discontinuities. *Astrophys. J. Lett.* **2013**, *772*, L14. [[CrossRef](#)]
14. Osman, K.T.; Matthaeus, W.H.; Gosling, J.T.; Greco, A.; Servidio, S.; Hnat, B.; Chapman, S.C.; Phan, T.D. Magnetic Reconnection and Intermittent Turbulence in the Solar Wind. *Phys. Rev. Lett.* **2014**, *112*, 215002. [[CrossRef](#)]
15. Kislov, R.A.; Khabarova, O.V.; Malova, H.V. Quasi-stationary current sheets of the solar origin in the heliosphere. *Astrophys. J.* **2019**, *875*, 28. [[CrossRef](#)]
16. Maiewski, E.V.; Malova, H.V.; Kislov, R.A.; Popov, V.Y.; Petrukovich, A.A.; Khabarova, O.V.; Zelenyi, L.M. Formation of multiple current sheets in the heliospheric plasma sheet. *Cosmic Res.* **2020**, *58*, 411–425. [[CrossRef](#)]
17. Khabarova, O.; Malandraki, O.; Malova, H.; Kislov, R.; Greco, A.; Bruno, R.; Pezzi, O.; Servidio, S.; Li, G.; Matthaeus, W.; et al. Current sheets, plasmoids and flux ropes in the heliosphere. Part I. 2-D or not 2-D? General and observational aspects. *Space Sci. Rev.* **2021**, *217*, 38. [[CrossRef](#)]
18. Khabarova, O.; Büchner, J.; Jain, N.; Sagitov, T.; Malova, H.; Kislov, R. Electron-to-ion Bulk Speed Ratio as a Parameter Reflecting the Occurrence of Strong Electron-dominated Current Sheets in the Solar Wind. *Astrophys. J.* **2022**, *933*, 97. [[CrossRef](#)]
19. Lazarian, A.; Vlahos, L.; Kowal, G.; Yan, H.; Beresnyak, A.; de Gouveia Dal Pino, E.M. Turbulence, magnetic reconnection in turbulent fluids and energetic particle acceleration. *Space Sci. Rev.* **2012**, *173*, 557–622. [[CrossRef](#)]
20. Eriksson, S.; Newman, D.L.; Lapenta, G.; Angelopoulos, V. On the signatures of magnetic islands and multiple X-lines in the solar wind as observed by ARTEMIS and WIND. *Plasma Phys. Contr. Fus.* **2014**, *56*, 064008. [[CrossRef](#)]
21. Khabarova, O.; Zank, G.P.; Li, G.; le Roux, J.A.; Webb, G.M.; Dosch, A.; Malandraki, O.E. Small-scale magnetic islands in the solar wind and their role in particle acceleration. I. Dynamics of magnetic islands near the heliospheric current sheet. *Astrophys. J.* **2015**, *808*, 181. [[CrossRef](#)]
22. Khabarova, O.; Zank, G.P.; Li, G.; Malandraki, O.E.; le Roux, J.A.; Webb, G.M. Small-scale magnetic islands in the solar wind and their role in particle acceleration. II. Particle energization inside magnetically confined cavities. *Astrophys. J.* **2016**, *827*, 122. [[CrossRef](#)]
23. Khabarova, O.V.; Zank, G.P. Energetic Particles of keV–MeV energies observed near reconnecting current sheets at 1 au. *Astrophys. J.* **2017**, *843*, 4. [[CrossRef](#)]
24. Adhikari, L.; Khabarova, O.; Zank, G.P.; Zhao, L.-L. The Role of Magnetic Reconnection-associated Processes in Local Particle Acceleration in the Solar Wind. *Astrophys. J.* **2019**, *873*, 72. [[CrossRef](#)]
25. Lazarian, A.; Eyink, G.L.; Jafari, A.; Kowal, G.; Li, H.; Xu, S.; Vishniac, E.T. 3D turbulent reconnection: Theory, tests, and astrophysical implications. *Phys. Plasmas* **2020**, *27*, 012305. [[CrossRef](#)]
26. Sundkvist, D.; Retinò, A.; Vaivads, A.; Bale, S.D. Dissipation in Turbulent Plasma due to Reconnection in Thin Current Sheets. *Phys. Rev. Lett.* **2007**, *99*, 025004. [[CrossRef](#)]
27. Vech, D.; Mallet, A.; Klein, K.G.; Kasper, J.C. Magnetic Reconnection May Control the Ion-scale Spectral Break of Solar Wind Turbulence. *Astrophys. J. Lett.* **2018**, *855*, L27. [[CrossRef](#)]
28. Franci, L.; Papini, E.; Micera, A.; Lapenta, G.; Hellinger, P.; Del Sarto, D.; Burgess, D.; Landi, S. Anisotropic Electron Heating in Turbulence-driven Magnetic Reconnection in the Near-Sun Solar Wind. *Astrophys. J.* **2022**, *936*, 27. [[CrossRef](#)]
29. Gomes, L.F.; Gomes, T.F.P.; Rempel, E.L.; Gama, S. Origin of multifractality in solar wind turbulence: The role of current sheets. *Monthly Notices of the R. Astr. Soc.* **2023**, *519*, 3623–3634. [[CrossRef](#)]
30. Karimabadi, H.; Roytershteyn, V.; Daughton, W.; Liu, Y.-H. Recent Evolution in the Theory of Magnetic Reconnection and its Connection with Turbulence. *Space Sci. Rev.* **2013**, *178*, 307–323. [[CrossRef](#)]
31. Karimabadi, H.; Roytershteyn, V.; Vu, H.X.; Omelchenko, Y.A.; Scudder, J.; Daughton, W.; Dimmock, A.; Nykyri, K.; Wan, M.; Sibeck, D.; et al. The link between shocks, turbulence, and magnetic reconnection in collisionless plasmas. *Phys. Plasmas* **2014**, *21*, 062308. [[CrossRef](#)]
32. Howes, G.G. A dynamical model of plasma turbulence in the solar wind. *Phil. Trans. R. Soc. A* **2015**, *373*, 20140145. [[CrossRef](#)] [[PubMed](#)]
33. Bruno, R. Intermittency in solar wind turbulence from fluid to kinetic scales. *Earth Space Sci.* **2019**, *6*, 656–672. [[CrossRef](#)]
34. Azizabadi, A.C.; Jain, N.; Büchner, J. Identification and characterization of current sheets in collisionless plasma turbulence. *Phys. Plasmas* **2021**, *28*, 052904. [[CrossRef](#)]
35. Raouafi, N.E.; Stenborg, G.; Seaton, D.B.; Wang, H.; Wang, J.; De Forest, C.E.; Bale, S.D.; Drake, J.F.; Uritsky, V.M.; Karpen, J.T.; et al. Magnetic Reconnection as the Driver of the Solar Wind. *Astrophys. J.* **2023**, *945*, 28. [[CrossRef](#)]
36. Li, G.; Miao, B.; Hu, Q.; Qin, G. Effect of current sheets on the solar wind magnetic field power spectrum from the Ulysses observation: From Kraichnan to Kolmogorov Scaling. *Phys. Rev. Lett.* **2011**, *106*, 125001. [[CrossRef](#)]
37. Borovsky, J.E.; Burkholder, B.L. On the Fourier contribution of strong current sheets to the high-frequency magnetic power spectral density of the solar wind. *J. Geophys. Res. Space Phys.* **2020**, *125*, e2019JA027307. [[CrossRef](#)]
38. Yordanova, E.; Vörös, Z.; Raptis, S.; Karlsson, T. Current sheet statistics in the magnetosheath. *Front. Astron. Sp. Sci.* **2020**, *7*, 2. [[CrossRef](#)]
39. Khabarova, O.; Sagitov, T.; Kislov, R.; Li, G. Automated identification of current sheets—A new tool to study turbulence and intermittency in the solar wind. *J. Geophys. Res. Space Phys.* **2021**, *126*, e2020JA029099. [[CrossRef](#)]
40. Alexandrova, O.; Chen, C.H.K.; Sorriso-Valvo, L.; Horbury, T.S.; Bale, S.D. Solar wind turbulence and the role of ion instabilities. *Space Sci. Rev.* **2013**, *178*, 101–139. [[CrossRef](#)]

41. Bruno, R.; Carbone, V. The solar wind as a turbulence laboratory. *Living Rev. Sol. Phys.* **2013**, *10*, 2. [[CrossRef](#)]
42. Riazantseva, M.O.; Budaev, V.P.; Zelenyi, L.M.; Zastenker, G.N.; Pavlos, G.P.; Safrankova, J.; Nemecek, Z.; Prech, L.; Nemec, F. Dynamic properties of small scale solar wind plasma fluctuations. *Phil. Trans. R. Soc. A* **2015**, *373*, 20140146. [[CrossRef](#)]
43. Šafránková, J.; Němeček, Z.; Němec, F.; Přejch, L.; Pitňa, A.; Chen, C.H.K.; Zastenker, G.N. Solar wind density spectra around the ion spectral break. *Astrophys. J.* **2015**, *803*, 107. [[CrossRef](#)]
44. Rakhmanova, L.; Riazantseva, M.; Zastenker, G. Plasma and Magnetic Field Turbulence in the Earth's Magnetosheath at Ion Scales. *Front. Astron. Space Sci.* **2021**, *7*, 616635. [[CrossRef](#)]
45. Alexandrova, O.; Saur, J.; Lacombe, C.; Mangeney, A.; Mitchell, J.; Schwartz, S.J.; Robert, P. Universality of solar-wind turbulent spectrum from MHD to electron scales. *Phys. Rev. Lett.* **2009**, *103*, 165003. [[CrossRef](#)]
46. Roberts, O.W.; Alexandrova, O.; Kajdic, P.; Turci, L.; Perrone, D.; Escoubet, C.P.; Walsh, A. Variability of the Magnetic Field Power Spectrum in the Solar Wind at Electron Scales. *Astrophys. J.* **2017**, *850*, 120. [[CrossRef](#)]
47. Sahraoui, F.; Goldstein, M.L.; Robert, P.; Khotyaintsev, Y. Evidence of a cascade and dissipation of solar-wind turbulence at the electron gyroscale. *Phys. Rev. Lett.* **2009**, *102*, 231102. [[CrossRef](#)]
48. Sahraoui, F.; Huang, S.Y.; Belmont, G.; Goldstein, M.L.; Réтино, A.; Robert, P.; De Patoul, J. Scaling of electron dissipation range of solar wind turbulence. *Astrophys. J.* **2013**, *777*, 15. [[CrossRef](#)]
49. Frisch, U. *Turbulence: The Legacy of A.N. Kolmogorov*; Cambridge University Press: Cambridge, UK; New York, NY, USA, 1995. [[CrossRef](#)]
50. Telloni, D.; Sorriso-Valvo, L.; Woodham, L.D.; Panasenco, O.; Velli, M.; Carbone, F.; Zank, G.P.; Bruno, R.; Perrone, D.; Nakanotani, M.; et al. Evolution of Solar Wind Turbulence from 0.1 to 1 au during the First Parker Solar Probe–Solar Orbiter Radial Alignment. *Astrophys. J. Lett.* **2021**, *912*, L21. [[CrossRef](#)]
51. Roberts, O.W.; Li, X.; Jeska, L. A statistical study of the solar wind turbulence at ion scales using the K-filtering technique and Cluster data. *Astrophys. J.* **2015**, *802*, 2. [[CrossRef](#)]
52. Kilpua, E.K.J.; Fontaine, D.; Good, S.W.; Ala-Lahti, M.; Osmane, A.; Palmerio, E.; Yordanova, E.; Moissard, C.; Hadid, L.Z.; Janvier, M. Magnetic field fluctuation properties of coronal mass ejection-driven sheath regions in the near-Earth solar wind. *ANGELO* **2020**, *38*, 999–1017. [[CrossRef](#)]
53. Sorriso-Valvo, L.; Yordanova, E.; Dimmock, A.P.; Telson, D.I. Turbulent cascade and energy transfer rate in a solar coronal mass ejection. *Astrophys. J. Lett.* **2021**, *919*, L30. [[CrossRef](#)]
54. Goldreich, P.; Sridhar, S. Toward a Theory of Interstellar Turbulence. II. Strong Alfvénic Turbulence. *Astrophys. J.* **1995**, *438*, 763. [[CrossRef](#)]
55. Schekochihin, A.A.; Cowley, S.C.; Dorland, W.; Hammett, G.W.; Howes, G.G.; Quataert, E.; Tatsuno, T. Astrophysical gyrokinetics: Kinetic and fluid turbulent cascades in magnetized weakly collisional plasmas. *Astrophys. J.* **2009**, *182*, 310. [[CrossRef](#)]
56. Boldyrev, S.; Perez, J.C. Spectrum of kinetic-Alfvén turbulence. *Astrophys. J. Lett.* **2012**, *758*, L44. [[CrossRef](#)]
57. Howes, G.G.; Cowley, S.C.; Dorland, W.; Hammett, G.W.; Quataert, E.; Schekochihin, A.A. A model of turbulence in magnetized plasmas: Implications for the dissipation range in the solar wind. *J. Geophys. Res. Space Phys.* **2008**, *113*, A05103. [[CrossRef](#)]
58. Riazantseva, M.O.; Rakhmanova, L.S.; Zastenker, G.N.; Yermolaev, Y.I.; Lodkina, I.G. Features of the Spectral Characteristics of Plasma Fluctuations in Different Large-Scale Streams of the Solar Wind. *Geom. Aeron.* **2019**, *59*, 127–135. [[CrossRef](#)]
59. Papini, E.; Cicone, A.; Franci, L.; Piersanti, M.; Landi, S.; Hellinger, P.; Verdini, A. Spacetime Hall-MHD Turbulence at Sub-ion Scales: Structures or Waves? *Astrophys. J. Lett.* **2021**, *917*, L12. [[CrossRef](#)]
60. Riazantseva, M.O.; Rakhmanova, L.S.; Yermolaev, Y.I.; Lodkina, I.G.; Zastenker, G.N.; Chesalin, L.S. Characteristics of Turbulent Solar Wind Flow in Plasma Compression Regions. *Cosm. Res.* **2020**, *58*, 468–477. [[CrossRef](#)]
61. Elliott, H.A.; McComas, D.J.; Schwadron, N.A.; Gosling, J.T.; Skoug, R.M.; Gloeckler, G.; Zurbuchen, T.H. An improved expected temperature formula for identifying interplanetary coronal mass ejections. *J. Geophys. Res. Space Phys.* **2005**, *110*, A04103. [[CrossRef](#)]
62. Zank, G.P.; Hunana, P.; Mostafavi, P.; Le Roux, J.A.; Li, G.; Webb, G.M.; Khabarova, O.; Cummings, A.; Stone, E.; Decker, R. Diffusive shock acceleration and reconnection acceleration processes. *Astrophys. J.* **2015**, *814*, 137. [[CrossRef](#)]
63. Shaikh, Z.I.; Raghav, A.N.; Vichare, G.; Bhaskar, A.; Mishra, W. Comparative statistical study of characteristics of plasma in planar and non-planar ICME sheaths during solar cycles 23 and 24. *Mon. Not. R. Astron. Soc.* **2020**, *494*, 2498–2508. [[CrossRef](#)]
64. Kilpua, E.K.J.; Good, S.W.; Ala-Lahti, M.; Osmane, A.; Pal, S.; Soljento, J.E.; Zhao, L.L.; Bale, S. Structure and fluctuations of a slow ICME sheath observed at 0.5 au by the Parker Solar Probe. *Astron. Astrophys.* **2022**, *663*, A108. [[CrossRef](#)]
65. Ghag, K.; Pathare, P.; Raghav, A.; Nicolaou, G.; Shaikh, Z.; Dhamane, O.; Panchal, U.; Kumbhar, K.; Tari, P.; Sathe, B.; et al. Studying the polytropic behavior of an ICME using Multi-spacecraft observation by STEREO-A, STEREO-B, and WIND. *Adv. Space Res.* **2024**, *73*, 1064–1072. [[CrossRef](#)]
66. Srivastava, N.; Mirtoshev, A.; Mishra, W. Investigating the variations in the composition and heating of interacting ICMEs. *Front. Astron. Space Sci.* **2023**, *10*, 1154612. [[CrossRef](#)]
67. Yermolaev, Y.I.; Nikolaeva, N.S.; Lodkina, I.G.; Yermolaev, M.Y. Catalog of Large-Scale Solar Wind Phenomena during 1976–2000. *Cosm. Res.* **2009**, *47*, 81–94. [[CrossRef](#)]
68. Nieves-Chinchilla, T.; Vourlidas, A.; Raymond, J.C.; Linton, M.G.; Al-haddad, N.; Savani, N.P.; Szabo, A.; Hidalgo, M.A. Understanding the internal magnetic field configurations of ICMEs using more than 20 years of Wind observations. *Solar Phys.* **2018**, *293*, 25. [[CrossRef](#)]

69. Ogilvie, K.W.; Chornay, D.J.; Fritzenreiter, R.J.; Hunsaker, F.; Keller, J.; Lobell, J.; Miller, G.; Scudder, J.D.; Sittler, E.C.; Torbert, R.B.; et al. SWE, a Comprehensive Plasma Instrument for the WIND Spacecraft. *Space Sci. Rev.* **1995**, *71*, 55–77. [[CrossRef](#)]
70. Lin, R.P.; Anderson, K.A.; Ashford, S.; Carlson, C.; Curtis, D.; Ergun, R.; Larson, D.; McFadden, J.; McCarthy, M.; Parks, G.K.; et al. A Three-Dimensional Plasma and Energetic Particle Investigation for the Wind Spacecraft. *Space Sci. Rev.* **1995**, *71*, 125–153. [[CrossRef](#)]
71. Lepping, R.P.; Acuña, M.H.; Burlaga, L.F.; Farrell, W.M.; Slavin, J.A.; Schatten, K.H.; Mariani, F.; Ness, N.F.; Neubauer, F.M.; Whang, Y.C.; et al. The WIND Magnetic Field Investigation. *Space Sci. Rev.* **1995**, *71*, 207–229. [[CrossRef](#)]
72. Alexandrova, O.; Carbone, V.; Veltri, P.; Soriso-Valvo, L. Small-scale energy cascade of the solar wind turbulence. *Astrophys. J.* **2008**, *674*, 1153. [[CrossRef](#)]
73. Jekel, C.F.; Venter, G. pwlif: A Python Library for Fitting 1D Continuous Piecewise Linear Functions. *Preprint* **2019**. [[CrossRef](#)]
74. Šafránková, J.; Němeček, Z.; Němec, F.; Verscharen, D.; Horbury, T.S.; Bale, S.D.; Přech, L. Evolution of Magnetic Field Fluctuations and Their Spectral Properties within the Heliosphere: Statistical Approach. *Astrophys. J. Lett.* **2023**, *946*, L44. [[CrossRef](#)]
75. Greco, A.; Perri, S.; Servidio, S.; Yordanova, E.; Veltri, P. The complex structure of magnetic field discontinuities in the turbulent solar wind. *Astrophys. J. Lett.* **2016**, *823*, L39. [[CrossRef](#)]
76. Bandyopadhyay, R.; Matthaeus, W.H.; Chasapis, A.; Russell, C.T.; Strangeway, R.J.; Torbert, R.B.; Giles, B.L.; Gershman, D.J.; Pollock, C.J.; Burch, J.L. Direct Measurement of the Solar-Wind Taylor Microscale using MMS Turbulence Campaign Data. *Astrophys. J.* **2020**, *899*, 63. [[CrossRef](#)]
77. Tessein, J.A.; Smith, C.W.; Vasquez, B.J.; Skoug, R.M. Turbulence associated with corotating interaction regions at 1 AU: Inertial and dissipation range magnetic field spectra. *J. Geophys. Res. Space Phys.* **2011**, *116*, A10104. [[CrossRef](#)]
78. Smith, C.W.; Tessein, J.A.; Vasquez, B.J.; Skoug, R.M. Turbulence associated with corotating interaction regions at 1 AU: Inertial range cross-helicity spectra. *J. Geophys. Res. Space Phys.* **2011**, *116*, A10103. [[CrossRef](#)]
79. Richardson, I.G. Solar wind stream interaction regions throughout the heliosphere. *Living Rev. Sol. Phys.* **2018**, *15*, 1. [[CrossRef](#)]
80. Pitňa, A.; Šafránková, J.; Němeček, Z.; Ďurovcová, T.; Kis, A. Turbulence Upstream and Downstream of Interplanetary Shocks. *Front. Phys.* **2021**, *8*, 626768. [[CrossRef](#)]

Disclaimer/Publisher’s Note: The statements, opinions and data contained in all publications are solely those of the individual author(s) and contributor(s) and not of MDPI and/or the editor(s). MDPI and/or the editor(s) disclaim responsibility for any injury to people or property resulting from any ideas, methods, instructions or products referred to in the content.